

SELF-CONSISTENT 3D SUPERNOVA MODELS FROM  $-7$  MINUTES TO  $+7$  SECONDS:  
A 1-BETHE EXPLOSION OF A  $\sim 19 M_{\odot}$  PROGENITOR

ROBERT BOLLIG,<sup>1</sup> NAVEEN YADAV,<sup>1,2</sup> DANIEL KRESSE,<sup>1,3</sup> HANS-THOMAS JANKA,<sup>1</sup> BERNHARD MÜLLER,<sup>4,5,6</sup> AND  
ALEXANDER HEGER<sup>4,5,7,8</sup>

<sup>1</sup>Max Planck Institute for Astrophysics, Karl-Schwarzschild-Str. 1, 85748 Garching, Germany

<sup>2</sup>Excellence Cluster ORIGINS, Boltzmannstr. 2, 85748 Garching, Germany

<sup>3</sup>Physik-Department, Technische Universität München, James-Frank-Str. 1, 85748 Garching, Germany

<sup>4</sup>School of Physics and Astronomy, Monash University, Victoria 3800, Australia

<sup>5</sup>Australian Research Council Centre of Excellence for Gravitational Wave Discovery (OzGrav), Clayton, VIC 3800, Australia

<sup>6</sup>Astrophysics Research Centre, School of Mathematics and Physics, Queen's University Belfast, BT7 1NN, Belfast, Northern Ireland

<sup>7</sup>Center of Excellence for Astrophysics in Three Dimensions (ASTRO-3D), Australia

<sup>8</sup>Joint Institute for Nuclear Astrophysics, 1 Cyclotron Laboratory, National Superconducting Cyclotron Laboratory, Michigan State University, East Lansing, MI 48824-1321, USA

(Received 00, 00, 2020; Revised 00, 00, 2020; Accepted 00, 00, 2020)

Submitted to ApJ

ABSTRACT

To date, modern three-dimensional (3D) supernova (SN) simulations have not demonstrated that explosion energies of  $10^{51}$  erg ( $= 1$  bethe  $= 1$  B) or more are possible for neutrino-driven SNe of non/slow-rotating  $M < 20 M_{\odot}$  progenitors. We present the first such model, considering a non-rotating, solar-metallicity  $18.88 M_{\odot}$  progenitor, whose final 7 minutes of convective oxygen-shell burning were simulated in 3D and showed a violent oxygen-neon shell merger prior to collapse. A large set of 3D SN-models was computed with the PROMETHEUS-VERTEX code, whose improved convergence of the two-moment equations with Boltzmann closure allows now to fully exploit the implicit neutrino-transport treatment. Nuclear burning is treated with a 23-species network. We vary the angular grid resolution and consider different nuclear equations of state and muon formation in the proto-neutron star (PNS), which requires six-species transport with coupling of all neutrino flavors across all energy-momentum groups. Elaborate neutrino transport was applied until  $\sim 2$  s after bounce. In one case the simulation was continued to  $> 7$  s with an approximate treatment of neutrino effects that allows for seamless continuation without transients. A spherically symmetric neutrino-driven wind does not develop. Instead, accretion downflows to the PNS and outflows of neutrino-heated matter establish a monotonic rise of the explosion energy until  $\sim 7$  s post bounce, when the outgoing shock reaches  $\sim 50,000$  km and enters the He-layer. The converged value of the explosion energy at infinity (with overburden subtracted) is  $\sim 1$  B and the ejected  $^{56}\text{Ni}$  mass  $\lesssim 0.087 M_{\odot}$ , both within a few 10% of the SN 1987A values. The final NS mass and kick are  $\sim 1.65 M_{\odot}$  and  $> 450 \text{ km s}^{-1}$ , respectively.

*Keywords:* Supernovae: general — supernovae: individual (SN 1987A) — neutrinos — hydrodynamics — instabilities

1. INTRODUCTION

Self-consistent 3D simulations with energy-dependent neutrino transport (e.g., Takiwaki et al. 2014; Melson et al. 2015b,a; Lentz et al. 2015; Ott et al. 2018; Janka et al. 2016; Summa et al. 2018; Müller et al. 2017a, 2019;

Burrows et al. 2020; Stockinger et al. 2020) have recently demonstrated the viability of the neutrino-driven mechanism (Colgate & White 1966; Arnett 1966; Bethe & Wilson 1985) for core-collapse supernovae (CCSNe), supporting earlier 3D results with gray neutrino transport and smoothed-particle hydrodynamics (Fryer & Warren 2002). Besides a detailed treatment of the crucial neutrino physics, modern grid-based hydrodynamics schemes are necessary for a reliable description of explosion-assisting hydrodynamic instabilities in the

form of convective overturn (Herant et al. 1994; Burrows et al. 1995; Janka & Müller 1996), the standing accretion shock instability (SASI; Blondin et al. 2003; Blondin & Mezzacappa 2007), and turbulent flows (e.g., Murphy et al. 2013; Couch & Ott 2015; Radice et al. 2016) in the postshock layer. Pre-collapse asymmetries in the convectively burning oxygen and silicon shells (Arnett & Meakin 2011; Couch et al. 2015; Müller et al. 2016b; Yadav et al. 2020; Yoshida et al. 2019) turned out to facilitate the onset of the explosion by strengthening the growth and power of postshock instabilities (Couch & Ott 2013; Müller & Janka 2015; Müller et al. 2017a). Moreover, moderate or rapid rotation (Fryer & Warren 2004; Summa et al. 2018; Kuroda et al. 2020; Obergaulinger & Aloy 2021), magnetic field effects also in non-rotating collapsing stellar cores (Müller & Varma 2020), or enhanced neutrino luminosities or harder neutrino spectra due to a faster contraction of the proto-neutron star (PNS) connected to microphysics (e.g., Melson et al. 2015a; Bollig et al. 2017; Yasin et al. 2020) can play a role in triggering an (earlier) beginning of the explosion.

An open problem still to be solved is the question about SN energies that can be reached by the neutrino-driven mechanism. In view of current self-consistent multi-D simulations that follow the post-bounce evolution for typically  $\lesssim 1$  s, concerns were expressed that the explosions might be under-energetic compared to observations (e.g., Papish et al. 2015; Murphy et al. 2019). But only for low-mass ( $\lesssim 10 M_{\odot}$ ) progenitors with very low core compactness (Kitaura et al. 2006; Melson et al. 2015b; Stockinger et al. 2020) and some ultra-stripped progenitors (e.g., Müller et al. 2019) this time scale may be sufficient to determine the final value of the explosion energy. For more massive progenitors with high mass-accretion rates of the PNS, however, it can take much longer for the energy to saturate. So far, only in axi-symmetry (2D) the corresponding explosions could be tracked sufficiently long to reach energy saturation (Müller 2015; Bruenn et al. 2016; Nakamura et al. 2019; Burrows & Vartanyan 2021). In 3D, the final values were still not saturated and well below 1 B (Müller et al. 2017a) and thus below the margin considered to be typical of common Type-II SN progenitors. Exceptions were only found for special, extremely rapidly rotating, strongly magnetized, or very massive black-hole forming stars (Kuroda et al. 2020; Obergaulinger & Aloy 2021; Chan et al. 2020; Powell & Müller 2020; Fujibayashi et al. 2021).

In this paper, we present the first self-consistent 3D simulations of a non-rotating progenitor in the typical mass range of CCSNe that yield an explosion with the canonical value near 1 B and an ejecta mass of  $^{56}\text{Ni}$  around the average amount (around  $0.05 M_{\odot}$ ; Müller et al. 2017b). We consider a solar-metallicity star of initially  $18.88 M_{\odot}$ , whose evolution was followed continuously in 3D through the final 7 minutes of convective

oxygen-shell burning, core collapse and bounce, until  $\sim 7$  s after core bounce, at which stage the shock passes the C/He interface and the explosion saturates at its final energy.

In Section 2 we briefly describe the considered progenitor model, numerical methods, and set of 3D simulations. In Section 3 we discuss our results with a focus on the influence of progenitor perturbations and resolution (Section 3.1), the evolution of the explosion asymmetry (Section 3.2), the explosion energy (Section 3.3), explosive nucleosynthesis (Section 3.4), and PNS properties (Section 3.5) in our longest simulation. In Section 4 we finish with our conclusions. Appendix A provides additional information on a subset of our larger sample of models for comparison, Appendix B reports on our investigation of the angular momentum evolution, and Appendix C contains additional details on the neutrino emission with respect to the electron-neutrino lepton-number emission asymmetry termed LESA).

## 2. MODELING SET-UP AND SIMULATIONS

### 2.1. Progenitor model

The  $18.88 M_{\odot}$  progenitor model was evolved with the implicit hydrodynamics code KEPLER in spherical symmetry (1D) until 7 minutes before iron-core collapse. At this stage it was mapped to the PROMETHEUS hydrodynamics code to follow the convective oxygen-shell burning for the final 7 minutes in 3D until the gravitational instability of the iron core set in (Yadav et al. 2020). The star was chosen because it lies in a mass regime where semi-analytic models (Müller et al. 2016a) and calibrated 1D simulations (Sukhbold et al. 2016) suggest high explosion energies by the neutrino-driven mechanism, and where a radially extended oxygen-burning shell is expected to favor low-mode (i.e., low spherical harmonics modes,  $\ell = 1, 2$ ) convection (Collins et al. 2018), which is most supportive for the onset of SN explosions (Müller & Janka 2015). Moreover, the progenitor’s initial mass and He-core mass ( $5.78 M_{\odot}$ ) are near those discussed for the progenitors of SN 1987A and Cassiopeia A (see, e.g., Utrobin et al. 2019 and Utrobin et al. 2021 for SN 1987A and Orlando et al. 2016 for Cassiopeia A). During the 3D simulation a vigorous O-Ne shell merger occurs in the convectively burning oxygen shell, leading to large-scale, large-amplitude asymmetries of density, velocity, and composition in the entire oxygen layer (for details, see Yadav et al. 2020). This perturbed state constitutes self-consistent initial conditions for the 3D core-collapse simulations reported in the present paper.

Ne-O shell mergers may not be an ubiquitous phenomenon in the mass range between  $15 M_{\odot}$  and  $20 M_{\odot}$ , but they can still occur in a significant fraction of progenitors (Rauscher et al. 2002; Sukhbold et al. 2018; Collins et al. 2018, who found them in about 40% of the cases in the mentioned mass range). In particular, around  $18 M_{\odot}$  there are large variations in the stellar

structure, almost chaotic, because of the transition of convective central C burning to radiative central C burning (Sukhbold et al. 2018; Sukhbold & Adams 2020). The fact that our model displays this phenomenon is interesting but not crucial for the success of explosion simulations. The relevant aspect in this context is the presence of large-scale convective perturbations of considerable amplitude in the inner burning shells prior to core collapse (see the discussions by Couch & Ott 2013 and Müller & Janka 2015). Such perturbations are predicted to be widespread in the convective O-shells of progenitors in the mentioned mass interval (Collins et al. 2018) and are not limited to cases with O-Ne shell mergers.

In the following we discuss results from a large set of new 3D core-collapse calculations, based on this  $18.88 M_{\odot}$  progenitor and conducted with the PROMETHEUS-VERTEX code. If started from the 3D initial data, these simulations reveal relatively weak sensitivity of the onset of the explosion to the high-density equation-of-state (EoS) of the PNS, the inclusion of muons, and also to the angular resolution, because the pre-collapse perturbations of the progenitor foster the development of violent postshock instabilities when the Si/O interface falls through the stagnant shock.

## 2.2. Numerical methods

The neutrino-hydrodynamics simulations presented here were performed with the PROMETHEUS-VERTEX code (Rampp & Janka 2002; Buras et al. 2006). PROMETHEUS-VERTEX is a pseudo-Newtonian neutrino-hydrodynamics code for 1D, 2D, and 3D CCSN simulations in polar coordinates. It employs an axis-free polar Yin-Yang grid (Wongwathanarat et al. 2010) and a Poisson solver for the components of a spherical harmonics expansion of the gravitational potential up to chosen order (Müller & Steinmetz 1995). The monopole is corrected for general relativistic effects according to Case A of Marek et al. (2006).

The PROMETHEUS module solves the equations of nonrelativistic hydrodynamics on an Eulerian grid (either fixed or moving). It is a higher-order, conservative, Godunov-type finite-volume scheme with an exact Riemann solver (Fryxell et al. 1991; Müller et al. 1991), which is based on the piecewise parabolic method (PPM) of Colella & Woodward (1984). It is supplemented by the consistent multifluid advection (CMA) scheme of Plewa & Müller (1999) to treat the advection of nuclear species in regions where nuclear statistical equilibrium (NSE) does not hold.

The VERTEX transport module solves the two-moment set of neutrino energy and momentum equations with a Boltzmann closure for the variable Eddington factor in the comoving frame of the stellar medium including all  $\mathcal{O}(v/c)$  terms ( $v$  is the fluid velocity,  $c$  the speed of light) as well as gravitational time dilation and redshifting (Rampp & Janka 2002). Multi-D aspects are

treated by the ray-by-ray-plus (RbR+) approximation (Buras et al. 2006), and the full set of neutrino interactions presented in these papers (including neutrino-neutrino scattering and pair conversion; Buras et al. 2003) is taken into account. The energy-momentum bins are coupled across the entire momentum space to treat inelastic effects in neutrino-lepton scatterings and in both neutral-current and charged-current neutrino-nucleon interactions. The last two are implemented by high-resolution rate tables including a random-phase approximation for nucleon correlations (Burrows & Sawyer 1998, 1999), weak-magnetism corrections (Horowitz 2002), and virial corrections for neutrino-nucleon scattering (Horowitz et al. 2017), smoothly connecting virial expansion results at low densities and random phase approximation results at high densities (C. Horowitz, private communication, 2016). Nucleon correlations and mean-field potentials (e.g., Reddy et al. 1998; Martínez-Pinedo et al. 2012) are implemented consistently with the employed EoS. Some of our models include muon physics in the EoS and in the neutrino transport (Bollig et al. 2017), in which case six-species transport of  $\nu_e$ ,  $\bar{\nu}_e$ ,  $\nu_{\mu}$ ,  $\bar{\nu}_{\mu}$ ,  $\nu_{\tau}$ ,  $\bar{\nu}_{\tau}$  instead of our standard four-species treatment (not discriminating  $\nu_{\mu}$  and  $\nu_{\tau}$ ) is applied.

Another new feature of the PROMETHEUS-VERTEX code is the fact that it contains an optimized version of the nuclear burning network XNet of Hix & Thielemann (1999a) now, which replaces the previous flashing treatment of Rampp & Janka (2002). Consistent with the tabulated NSE composition applied at temperatures  $T \geq 0.689$  MeV and densities  $\rho \leq 10^{11}$  g cm $^{-3}$  after bounce, it includes 23 nuclear species (neutrons, protons, deuterium, tritium,  $^3\text{He}$ ,  $^4\text{He}$ , the 12  $\alpha$ -nuclei from  $^{12}\text{C}$  to  $^{56}\text{Ni}$ ,  $^{14}\text{N}$ ,  $^{54}\text{Mn}$ ,  $^{56}\text{Fe}$ ,  $^{60}\text{Fe}$ ,  $^{70}\text{Ni}$ ), coupled by  $\alpha$ -reactions.

Network and VERTEX transport were used for evolution periods of  $\lesssim 2$  s after bounce. One 3D model was continued beyond that time by replacing VERTEX with a cheaper heating and cooling (HC) scheme described in detail in Stockinger et al. (2020) and, after a transition period of another  $\sim 0.1$  s, by applying NSE down to  $T = 0.343$  MeV instead of using the nuclear network.<sup>1</sup> This permitted a nearly transient-free and computationally much cheaper prolongation of the simulated evolution. Free parameters in the HC treatment were determined from a 1D PNS cooling simulation of the same 3D SN model, using PROMETHEUS-VERTEX.

The large set of 3D calculations that partly cover long evolution periods has become possible by a considerable computational acceleration of the original PROMETHEUS-VERTEX code implemented by Rampp

<sup>1</sup> This lower limit for the NSE description was only applied for high-entropy material with  $s/k_{\text{B}} > 6.5$ , whereas in lower-entropy regions of the infalling O+Ne layer and parts of the O+C layer the lower temperature limit for NSE was set to 0.5 MeV (see Section 3.1 of Stockinger et al. 2020).

**Table 1.** Summary of 3D CCSN simulations.

Model Name <sup>a</sup>	$t_{\text{bounce}}^b$ [ms]	$t_{\text{pb}}^{\text{exp}}$ [ms]	$t_{\text{pb}}^f$ [ms]	$M_{\text{PNS,b}}^f$ [ $M_{\odot}$ ]	$M_{\text{PNS,g}}^f$ [ $M_{\odot}$ ]	$R_{\text{PNS}}^f$ [km]	$E_{\text{exp}}^{\text{diag}}$ [B]	$E_{\text{exp}}^{\text{OB-}}$ [B]	$R_s^{270\text{ms}}$ [km]	$R_s^f$ [km]
H_P1D_LS220_m-	357		288						$107_{96}^{120}$	$98_{89}^{107}$
H_P3D_LS220_m-	357		285						$158_{114}^{213}$	$168_{120}^{245}$
M_P1D_LS220_m-	357	$\emptyset$	579	1.8788	1.8115	26.00	$\emptyset$	$\emptyset$	$142_{122}^{170}$	$82_{64}^{95}$
M_P3D_LS220_m-	357	418	1675	1.8655	1.7548	17.89	0.5071	0.2024	$165_{126}^{213}$	$9704_{7852}^{12203}$
<b>M_P3D_LS220_m-HC</b>	$\emptyset$	$\emptyset$	<b>7035</b>	<b>1.8654</b>	<b>1.6749</b>	<b>13.57</b>	<b>0.9779</b>	<b>0.9411</b>	$\emptyset$	<b><math>49470_{38333}^{66024}</math></b>
M_P3D_SFHo_m-	362	426	545	1.8635	1.8025	28.97	0.0184	-0.3978	$156_{122}^{206}$	$549_{251}^{948}$
L_P1D_LS220_m-	357	$\emptyset$	489	1.8503	1.7910	27.96	$\emptyset$	$\emptyset$	$173_{141}^{213}$	$81_{70}^{96}$
L_P3D_LS220_m-	357	400	1884	1.8530	1.7359	17.41	0.6314	0.3728	$159_{136}^{190}$	$11996_{9425}^{15332}$
L_P1D_SFHo_m-	362	$\emptyset$	486	1.8302	1.7798	30.12	$\emptyset$	$\emptyset$	$148_{128}^{169}$	$87_{67}^{108}$
L_P3D_SFHo_m-	362	602	742	1.9154	1.8399	25.27	0.1001	-0.2994	$162_{141}^{184}$	$1254_{545}^{1933}$
M_P1D_LS220_m+	357	$\emptyset$	321	1.8100	1.7646	31.32	$\emptyset$	$\emptyset$	$144_{126}^{170}$	$109_{201}^{124}$
M_P3D_LS220_m+	357	338	395	1.8235	1.7722	29.45	0.0137	-0.4140	$170_{133}^{213}$	$398_{201}^{719}$
M_P3D_SFHo_m+	362	379	430	1.8416	1.7875	30.46	0.0063	-0.4220	$154_{121}^{195}$	$319_{179}^{590}$
L_P1D_LS220_m+	357	$\emptyset$	391	1.8250	1.7734	29.33	$\emptyset$	$\emptyset$	$151_{120}^{185}$	$80_{85}^{95}$
L_P3D_LS220_m+	357	376	694	1.8971	1.8212	22.91	0.2316	-0.1613	$172_{136}^{201}$	$2726_{1767}^{3590}$
L_P1D_SFHo_m+	362	$\emptyset$	270	1.7889	1.7487	36.23	$\emptyset$	$\emptyset$	$139_{117}^{165}$	$137_{119}^{156}$
L_P3D_SFHo_m+	362	426	515	1.8668	1.8053	28.14	0.0306	-0.3899	$135_{115}^{174}$	$621_{298}^{910}$

<sup>a</sup>Naming convention: H (1°), M (2°), L (4°), P1D (1D progenitor), P3D (3D progenitor), LS220 (EoS of [Lattimer & Swesty 1991](#)), SFHo (EoS of [Hempel & Schaffner-Bielich 2010](#); [Steiner et al. 2013](#)), m- (without muons), m+ (with muons), and the suffix HC and blue color indicate the simulation that continues model M\_P3D\_LS220\_m- after 1.675s and uses the heating and cooling scheme instead of the VERTEX neutrino transport. Names of models with determined explosion times are boldfaced.

<sup>b</sup> $t_{\text{bounce}}$  is the time from the onset of core collapse until bounce;  $t_{\text{pb}}^{\text{exp}}$  is the post-bounce time when the explosion sets in, defined as the instant when the maximum shock radius reaches 400 km;  $t_{\text{pb}}^f$  is the post-bounce time when the simulation was terminated;  $M_{\text{PNS,b}}^f$  is the baryonic PNS mass at that time,  $M_{\text{PNS,g}}^f$  the corresponding gravitational mass,  $R_{\text{PNS}}^f$  the corresponding PNS radius (all of these PNS quantities are defined where the average density is  $10^{11} \text{ g cm}^{-3}$ );  $E_{\text{exp}}^{\text{diag}}$  is the diagnostic explosion energy of all ejected postshock matter with positive total energy at  $t_{\text{pb}}^f$ ,  $E_{\text{exp}}^{\text{OB-}}$  the corresponding net explosion energy, where the “overburden” of the gravitational binding energy of stellar matter ahead of the SN shock is subtracted, and  $R_s^{270\text{ms}}$  and  $R_s^f$  are the shock radii (average<sub>minimum</sub><sup>maximum</sup> values) at  $t_{\text{pb}} = 270 \text{ ms}$  and  $t_{\text{pb}}^f$ , respectively. Blank spaces indicate values that could not be determined yet, whereas  $\emptyset$  symbols correspond to values that do not exist for the given model.

& [Janka \(2002\)](#) and [Buras et al. \(2006\)](#) through a rigorous optimization of vectorization and parallelization for the new SuperMUC-NG architecture.<sup>2</sup> Moreover, improved convergence of the transport module permits now full exploitation of the implicit nature of the transport solver in computing the transport with time steps up to  $\sim 10^{-5} \text{ s}$ , which is 100 times bigger than the typical hydrodynamics steps. This was achieved by improved accuracy of the Jacobian matrix through a higher precision in the calculation of the partial derivatives. Moreover, the numerical stability in solving the model-Boltzmann equation was improved at steep discontinuities in energy space that are caused by Doppler

shifting at shocks. These occur mainly in narrowly localized regions in space and time when fast downflows hit the PNS surface. The enhanced stability and thus reduced number of iterations could be accomplished by spreading velocity jumps seen by the transport solver over a few more zones than computed for the stellar medium by the hydrodynamics module. In addition, a predictor-corrector scheme was implemented for treating the neutrino source terms in the hydrodynamics solver at 2<sup>nd</sup> order accuracy, thus increasing accuracy and stability for long transport time steps.

The use of large transport time steps in combination with much smaller time steps for the hydrodynamics has been tested extensively in 1D. Even beyond the factor of 100 mentioned above, this did not lead to any visible differences in the evolution. There are several reasons

<sup>2</sup> <https://doku.lrz.de/display/PUBLIC/SuperMUC-NG>

why the results are not sensitive to increased transport times: First, the conditions for neutrino transport are close to steady-state during most of the post-bounce evolution after shock stagnation. Second, the time scales for changes in the stellar medium connected to neutrino-transport source terms are usually much longer than the typical length of the time steps for the hydrodynamics solver, which are constrained by the short sound travel time (determining the Courant-Friedrich-Lewy (CFL) condition). Both aspects in combination also imply that changes of the background medium during each hydrodynamics time step are usually very small and have little effect on the exact solution of the transport problem. Third, we apply the neutrino source terms not at once but in fractions during each hydrodynamics step. In multi-D we do not expect any fundamental differences and more serious intricacies, although short periods of time occur where fast downflows penetrate to the PNS and the neutrino radiation field can become non-stationary. However, during these periods also the transport time steps tend to become smaller and the transport is therefore well able to follow the faster changes of the neutrino distributions in space and momentum space. Inside the PNS, where neutrinos are strongly coupled to the fluid, the flow is no longer as close to hydrostatic equilibrium as in 1D. The far subsonic flow implies, however, that the neutrino radiation field will still change on time scales that are  $\mathcal{O}(10^2)$  longer than the CFL time step. We stress that detailed and conclusive tests are much more difficult in multi-D than in 1D because of the nature of turbulent plasma flows, whose stochastic and chaotic behavior can be influenced by any small(er) changes in the coupling between hydrodynamics and neutrinos as well as any other changes of the physics inputs, grid structure and resolution, besides the time stepping procedure used in the numerical codes.

### 2.3. Model simulations

We performed CCSN simulations with the nuclear EoS of Lattimer & Swesty (1991) with an incompressibility modulus of  $K = 220$  MeV (LS220) and the SHFo EoS of Hempel & Schaffner-Bielich (2010) and Steiner et al. (2013) with  $K = 245$  MeV, applied before core bounce in the NSE regime and after core bounce at densities above  $10^{11}$  g cm $^{-3}$ . We consider models with angular resolutions of  $4^\circ$  (“low”; L-models),  $2^\circ$  (“medium”; M-models), and  $1^\circ$  (“high”; H-models). We used a moving radial grid during the pre-bounce infall, and a Eulerian grid of initially 550 radial zones with geometric spacing (resolution  $\Delta r/r < 0.028$  everywhere) out to 60,000 km after bounce (open outer boundary), covering the entire perturbed O-shell, where large convective asymmetries were present (up to a mass coordinate of  $\sim 4.2 M_\odot$  and radius of 45,000 km). To resolve the steepening density gradient at the PNS surface, the radial grid was successively refined until it had 755 grid points with a mini-

mum of  $\Delta r/r = 0.002$ . The central 3 km (1.6 km until  $\sim 1$  s post bounce) were calculated in spherical symmetry to improve stability and reduce the time-step constraint for the explicit hydrodynamics module. The neutrino spectrum was discretized with 15 geometrically-spaced energy bins for  $0 \leq \epsilon_\nu \leq 380$  MeV.

For the long-time run with the HC scheme we extended the radial grid to approximately 100,000 km with  $\Delta r/r \sim 0.01$ . To regain computational efficiency we slightly coarsened the radial grid in the PNS interior and also increased the 1D core from the final value of 3 km in the VERTEX runs to roughly 15 km in the continuation calculation with the HC treatment (see Appendix E of Stockinger et al. 2020).

We provide an overview of all models in Table 1. The models are sorted and named by their H, M, or L resolution; P1D or P3D denote 1D or 3D pre-collapse conditions; LS220 and SFHo correspond to the employed high-density EoS; and m- and m+ mean computations without and with muons, respectively. Starting our simulations from 1D progenitors requires the use of artificial perturbations in order to seed the growth of nonradial hydrodynamic instabilities (otherwise the models preserve spherical symmetry during their evolution). Following our previous works for reasons of comparison, we applied the standard procedure used in PROMETHEUS-VERTEX simulations for this purpose, namely we imposed random cell-by-cell density perturbations imposed at bounce in the entire computational domain with an amplitude of 0.1% of the local average density.

We emphasize that in the current paper we will confine our discussion mainly to the two models with the longest simulated periods of evolution, namely L\_P3D\_LS220\_m- with  $4^\circ$  angular resolution and M\_P3D\_LS220\_m- (and its extension M\_P3D\_LS220\_m-HC) with  $2^\circ$  angular resolution, because these models permit the prediction of astronomically relevant explosion and remnant properties. As for most of the other models listed in Table 1, we will refer only to a few basic aspects connected to a subset of the cases or to some relevant entries in the table. These aspects shall allow the reader to judge the two highlighted models in the broader context of our entire sample of 3D simulations. More information on the models not further considered here will be presented in a follow-up paper.

## 3. RESULTS

### 3.1. Dependencies on progenitor perturbations, resolution, and microphysics

Our simulations starting from 1D pre-collapse conditions do not develop favorable conditions for an explosion, because the shock radius contracts quickly after reaching a maximum at  $\sim 200$  ms post bounce, when the infalling Si/O interface has crossed the shock. Strong SASI motions of the postshock layer lead to large-amplitude, quasi-periodic shock expansion and contraction episodes in all of these cases (see Figure A1 in Ap-

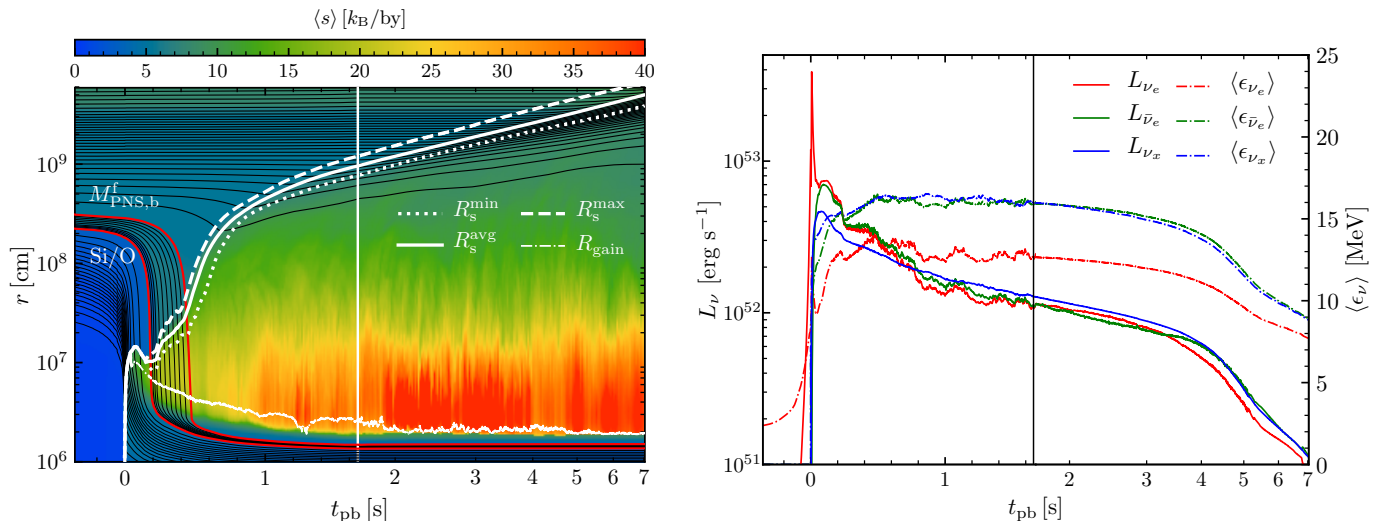


**Figure 1.** Explosion dynamics and neutrino emission of model M\_P3D\_LS220\_m- and its extension M\_P3D\_LS220\_m-HC. The time axes are chosen for optimal visibility. *Left:* Mass shells with entropy per nucleon color-coded. Maximum, minimum, and average shock radii, gain radius, and the mass shells of Si/O shell interface and final NS mass are marked. The vertical white line separates VERTEX transport (left, time linear) and HC neutrino approximation (right, time logarithmic). *Right:* Emitted luminosities and mean energies of  $\nu_e$ ,  $\bar{\nu}_e$ , and a single species of heavy-lepton neutrinos. The time axis is split as in the left panel. Right of the vertical solid line we show neutrino data from the artificially exploded 1D simulation.

pendix A and Glas et al. 2019b for a detailed discussion of similar behavior in non-exploding  $20 M_{\odot}$  simulations).

In contrast, all models with 3D initial conditions exhibit a phase of quasi-continuous shock expansion at  $t_{\text{pb}} \gtrsim 200$  ms and explode, if followed long enough (see models with boldfaced names in Table 1). In these cases, the infall of the large-amplitude density and velocity perturbations in the convective O-shell fosters vigorous convection as the dominant hydrodynamic instability in the gain layer behind the shock (discussed in detail by, e.g., Müller et al. 2017a; Müller & Janka 2015; Couch & Ott 2013). The typically larger shock radii in models started from 3D progenitor conditions can be verified for 270 ms post bounce (the latest common time of all models) in Table 1 and for a subset of models in Figure A1.

For L-models the shock-radius difference at 270 ms after bounce is reduced or even reversed (in L\_P1D\_LS220\_m- compared to L\_P3D\_LS220\_m-, and L\_P1D\_SFHo\_m+ compared to L\_P3D\_SFHo\_m+) because here the models started from the 1D progenitor develop stronger and longer-lasting SASI activity, aided by a lack of resolution to follow in detail the growth of Rayleigh-Taylor and Kelvin-Helmholtz (“parasitic”) instabilities. Such secondary instabilities tap energy from the coherent large-amplitude, large-scale SASI motions and thus limit the nonlinear saturation amplitude of the SASI (Guilet et al. 2010). The latter authors argued that a resolution of about  $2^{\circ}$  or better may be needed to resolve the relevant scales of the flow structures at the onset of their growth, and  $4^{\circ}$  or coarser may not suffice. Such quantitative statements, however, depend on the quality of the hydrodynamics solver, in particular on the order of

the employed discretization scheme, and therefore have to be investigated for each numerical code specifically.

Based on the resolution study performed with the PROMETHEUS code by Melson et al. (2020), one may expect that our  $2^{\circ}$  simulations are close to convergence in their global behavior (although local effects and short-time variations are always subject to changes when turbulent flows play a role), whereas the  $4^{\circ}$  models might hardly provide sufficient resolution to achieve convergence. In that study, however, 1D initial conditions were employed and our default small-amplitude random perturbations were applied to seed the convection, which in those models was the dominant postshock instability instead of SASI. Employing 3D progenitor data changes the growth conditions for postshock convection fundamentally. In Figure A1 all models started from the 3D progenitor (L\_P3D\_LS220\_m-, M\_P3D\_LS220\_m-, and H\_P3D\_LS220\_m-) exhibit a similar evolution of the average shock radius, independent of their angular resolution. In these models convection dominates in the postshock layer, too, but convergence (in the sense of overall similarity in the evolution) is fostered by the 3D progenitor asymmetries, which act as strong drivers of the hydrodynamic instabilities in the postshock volume. In contrast, models started from the 1D progenitor, where SASI becomes the dominant nonradial instability in the postshock layer, exhibit the resolution dependence discussed by Guilet et al. (2010). These models still display differences between the  $1^{\circ}$  and  $2^{\circ}$  simulations with the tendency of smaller shock radii and less vigorous SASI activity with better resolution (Figure A1). Therefore  $1^{\circ}$  models would be preferable for these conditions, but

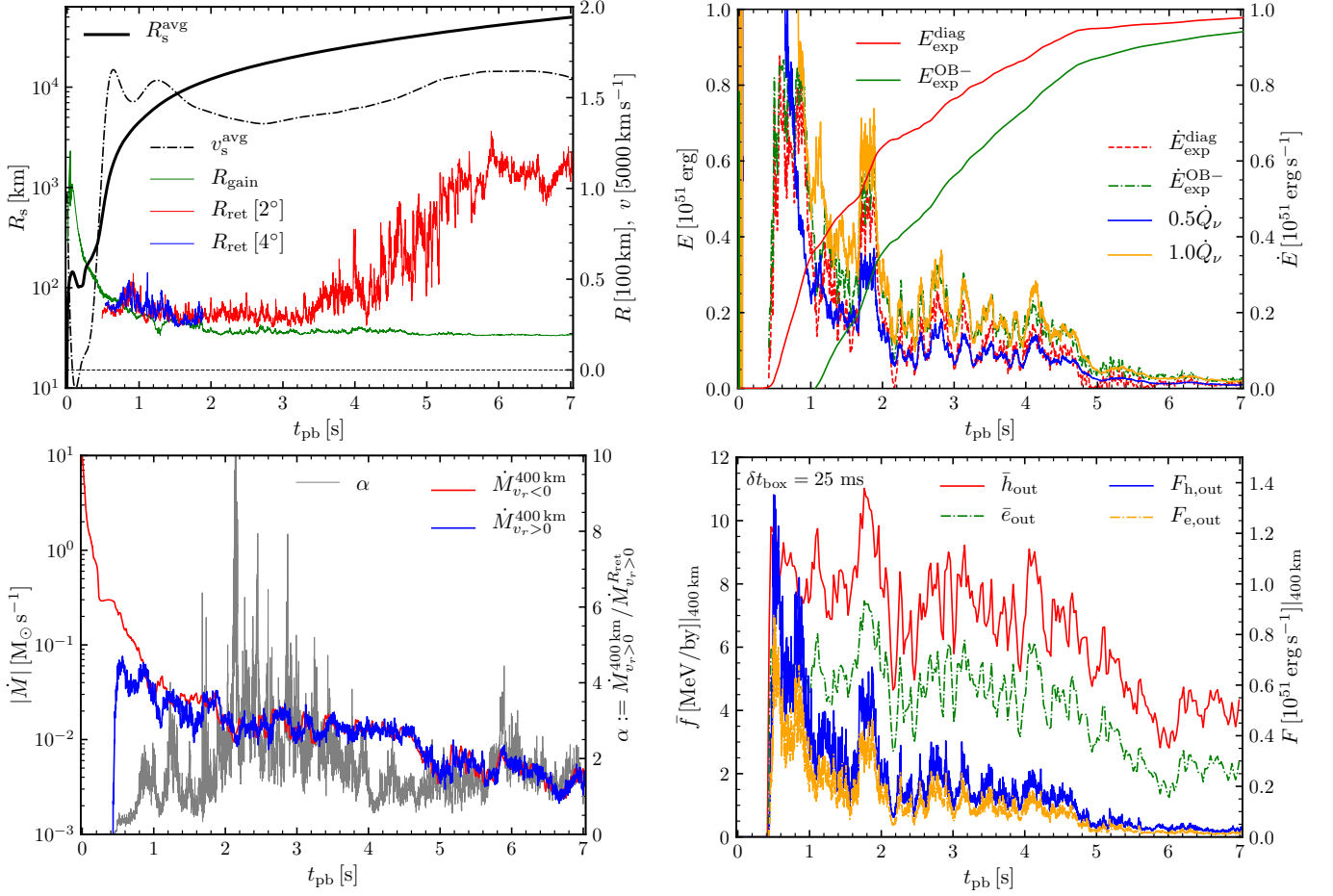


**Figure 2.** Evolution of explosion dynamics and explosion energy of model M.P3D\_LS220\_m- and its extension M.P3D\_LS220\_m-HC. *Top left:* Average values of shock radius and velocity, gain radius, and turnaround radius  $R_{\text{ret}}$  for model M.P3D\_LS220\_m- and its HC extension (both of which possess  $2^\circ$  angular resolution). For comparison, we also plot  $R_{\text{ret}}$  for model L.P3D\_LS220\_m- (having  $4^\circ$  angular resolution). *Top right:* Explosion energy, diagnostic and without overburden (OB-), and corresponding time derivatives compared to 0.5 and 1.0 of the net neutrino heating rate in the gain layer. At 7 s  $E_{\text{exp}}^{\text{OB-}}$  is still growing with a rate of  $\sim 0.02 \text{ B s}^{-1}$ . *Bottom left:* Mass accretion rate in downflows and ejection rate in outflows at 400 km, and ratio  $\alpha$  of the mass outflow rates at 400 km and at the average turnaround radius  $R_{\text{ret}}$ . *Bottom right:* Total enthalpy and energy fluxes,  $F_{\text{h,out}}$  and  $F_{\text{e,out}}$ , in outflows at 400 km and corresponding mean enthalpy and energy per baryon, averaged over a running window of 25 ms to reduce fluctuation amplitudes.

are practically not feasible with the computing resources available to us.

The onset of the explosion is measured by the time when the maximum shock radius reaches 400 km. Lower resolution (in the L-cases) may tend to delay the explosion compared to the M-cases (for as much as 176 ms in L.P3D\_SFHo\_m-), although M.P3D\_LS220\_m- and L.P3D\_LS220\_m- are exceptions as mentioned above. The tendency of earlier and faster explosions in 3D simulations with higher resolution has been demonstrated before with the PROMETHEUS code by Melson et al. (2020) and with FORNAX, another SN code using spherical polar coordinates, by Nagakura et al. (2019) and Burrows et al. (2020). This trend is typical of models where convective mass motions instead of SASI are the dominant nonradial hydrodynamic instability in the post-

shock layer. The trend is opposite when SASI dominates in the postshock layer. Under such circumstances the average shock radii are found to be smaller with higher resolution (see Figure A1 for an example), because the aforementioned influence of the parasitic instabilities reduces the saturation amplitude of the SASI by tapping energy from the coherent SASI mass motions. Smaller shock radii and delayed explosions with higher spatial resolution are also witnessed in 3D simulations of models with turbulent convection as the leading postshock instability when Cartesian grids are employed (see Radice et al. 2016). The reason for this finding could be smaller grid-induced perturbations with finer Cartesian grids, an effect that inhibits the instigation of postshock convection by such perturbations (for a detailed discus-

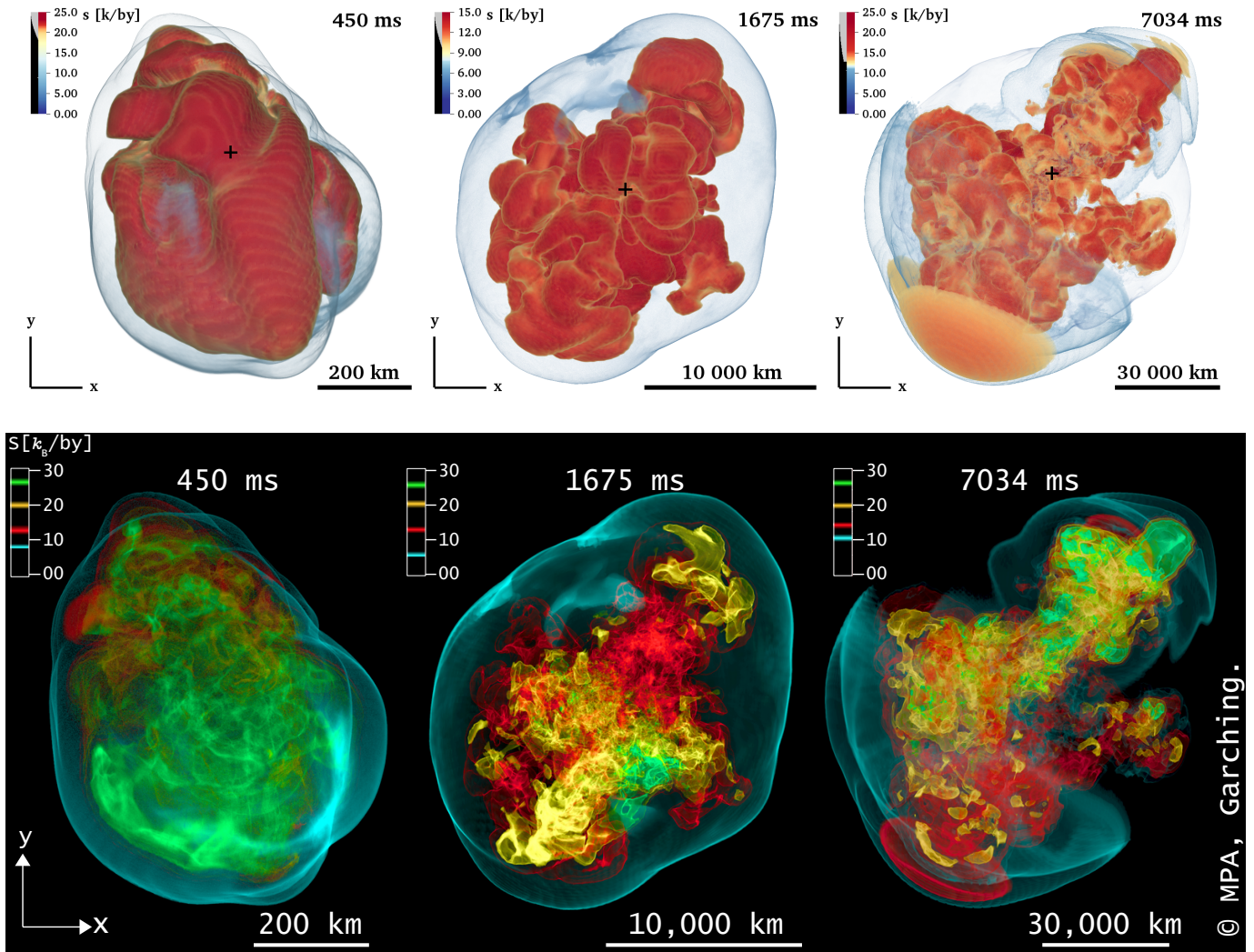


**Figure 3.** 3D explosion geometry of model M\_P3D\_LS220\_m- and its extension M\_P3D\_LS220\_m-HC. *Top row:* 3D volume renderings of plumes of high-entropy neutrino-heated matter viewed from the  $+z$ -direction at 0.450 s (just after the onset of the explosion), 1.675 s (at the end of the simulation with VERTEX neutrino transport), and 7.034 s (end of the simulation with HC neutrino approximation) after core bounce. The enveloping, transparent, bluish surface is the SN shock. The black cross marks the position of the PNS. At 7.034 s the shock has entered the He-layer and the entropy per baryon of postshock matter and neutrino-heated gas become similar. *Bottom row:* Volume renderings with higher transparency to allow for the better visibility of turbulent structures. The times, viewing directions, and scales are the same as in the panels of the upper row.

sion of such resolution dependent aspects, see also [Janka et al. 2016](#) and [Melson et al. 2020](#)).

In our set of models the shock runaway signalling the beginning of the explosion occurs somewhat later ( $\sim 10$ – $200$  ms) when using the SFHo EoS instead of the LS220 EoS, because with the latter nuclear EoS the hot PNS contracts faster during the first several 100 ms after bounce. The correspondingly hotter neutrinosphere leads to higher neutrino luminosities and harder neutrino spectra, both of which enhance the postshock neutrino heating and thus support earlier explosions (in line with results presented in, e.g., [Janka 2012](#); [Suwa et al. 2013](#)). For the same reason explosions set in earlier

( $\sim 25$ – $175$  ms) when muons are included (as first demonstrated by [Bollig et al. 2017](#)), where the biggest shifts are witnessed in L-models (Table 1).

The rest of our report is intended to be focused on the long-time evolution towards energy saturation and the corresponding changes of the nucleosynthetic composition in the shock-heated and neutrino-heated ejecta, both of which are observationally relevant. This aim naturally centers our entire discussion on model M\_P3D\_LS220\_m-, its extension M\_P3D\_LS220\_m-HC, and their lower-resolution counterpart L\_P3D\_LS220\_m-. The available computing resources did not permit us to continue all 3D runs to similarly late evolution stages,



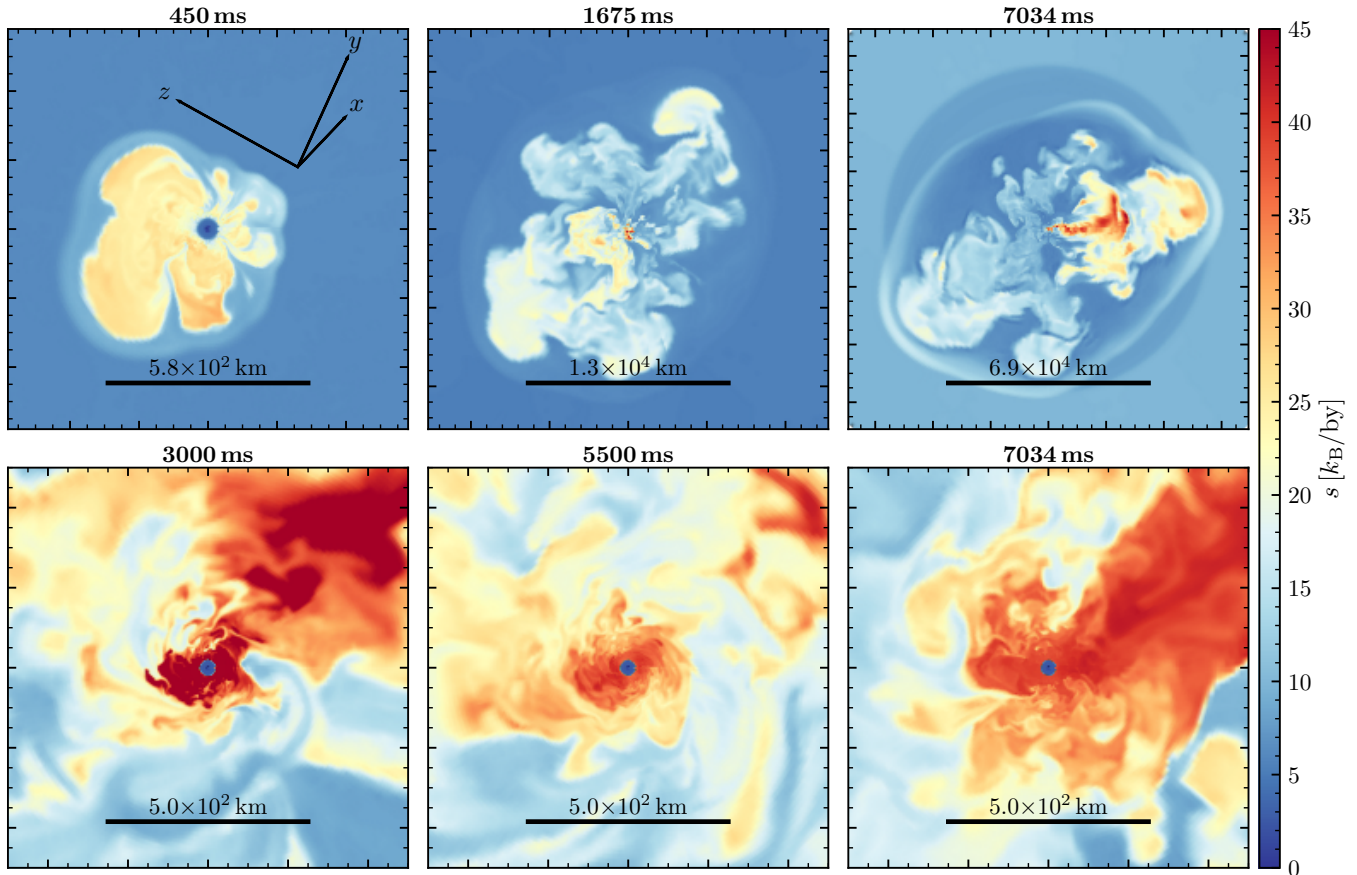


**Figure 4.** Explosion and accretion geometry of model `M_P3D_LS220_m-` and its extension `M_P3D_LS220_m-HC`. *Top row:* Entropy per baryon color-coded in a cross-sectional plane at 0.45 s, 1.675 s, and 7.034 s after bounce, rotated by roughly  $90^\circ$  relative to the orientation of the images in Figure 3. *Bottom row:* Close-ups of the turbulent vicinity of the PNS at 3.00 s, 5.50 s, and 7.034 s after bounce, showing lower-entropy downflows and high-entropy outflows of neutrino-heated matter. A spherical neutrino-driven wind does not develop until  $>7$  s after bounce.

for which reason our high-resolution (H) models offer information limited to only  $\sim 290$  ms after bounce, i.e., to a period before the onset of the explosion. For the same reason we could not conduct long-time evolution simulations for the SFHo EoS and for models including muons. This is unfortunate because SFHo is a more modern nuclear EoS, and the models including muons have the more complete microphysics, but they are also computationally significantly more expensive. We therefore decided to report additional results only of simulations with the LS220 EoS and without muon physics in the present paper. We refer the reader to a follow-up paper for details on the results of our simulations with muons and the two versions of the nuclear EoS until about 750 ms after bounce.

### 3.2. *O*-shell perturbations, shock revival, and explosion asymmetry

We mainly concentrate on the  $2^\circ$  model `M_P3D_LS220_m-`, which was followed with PROMETHEUS-VERTEX until 1.675 s after bounce, and compare some aspects with the

$4^\circ$  model `L_P3D_LS220_m-`, whose evolution was tracked until 1.884 s, also using the VERTEX neutrino transport. By applying the neutrino-HC scheme mentioned in Section 2.2, we continued model `M_P3D_LS220_m-` (maintaining  $2^\circ$  angular resolution) from 1.675 s until 7.035 s, when the shock had entered the He-layer at  $r = 52,000$  km and an enclosed mass of  $4.45 M_\odot$ , with a velocity of  $\sim 8,000$  km s $^{-1}$  (Figures 1 and 2). The run extended from 1.675 s to 7.035 s is named `M_P3D_LS220_m-HC` in Table 1.

`M_P3D_LS220_m-` and `L_P3D_LS220_m-` employ the same microphysics (LS220 EoS and no muons), are both based on the 3D progenitor model, and differ only in their angular resolutions. In Appendix A we compare the evolution of their average shock radii as functions of time. We also show these results for the corresponding 1D SN runs, without and with artificial explosion, and for the 3D SN runs of `L_P1D_LS220_m-`, and `M_P1D_LS220_m-`, all of which were started from the 1D progenitor data. Moreover, the two high-resolution

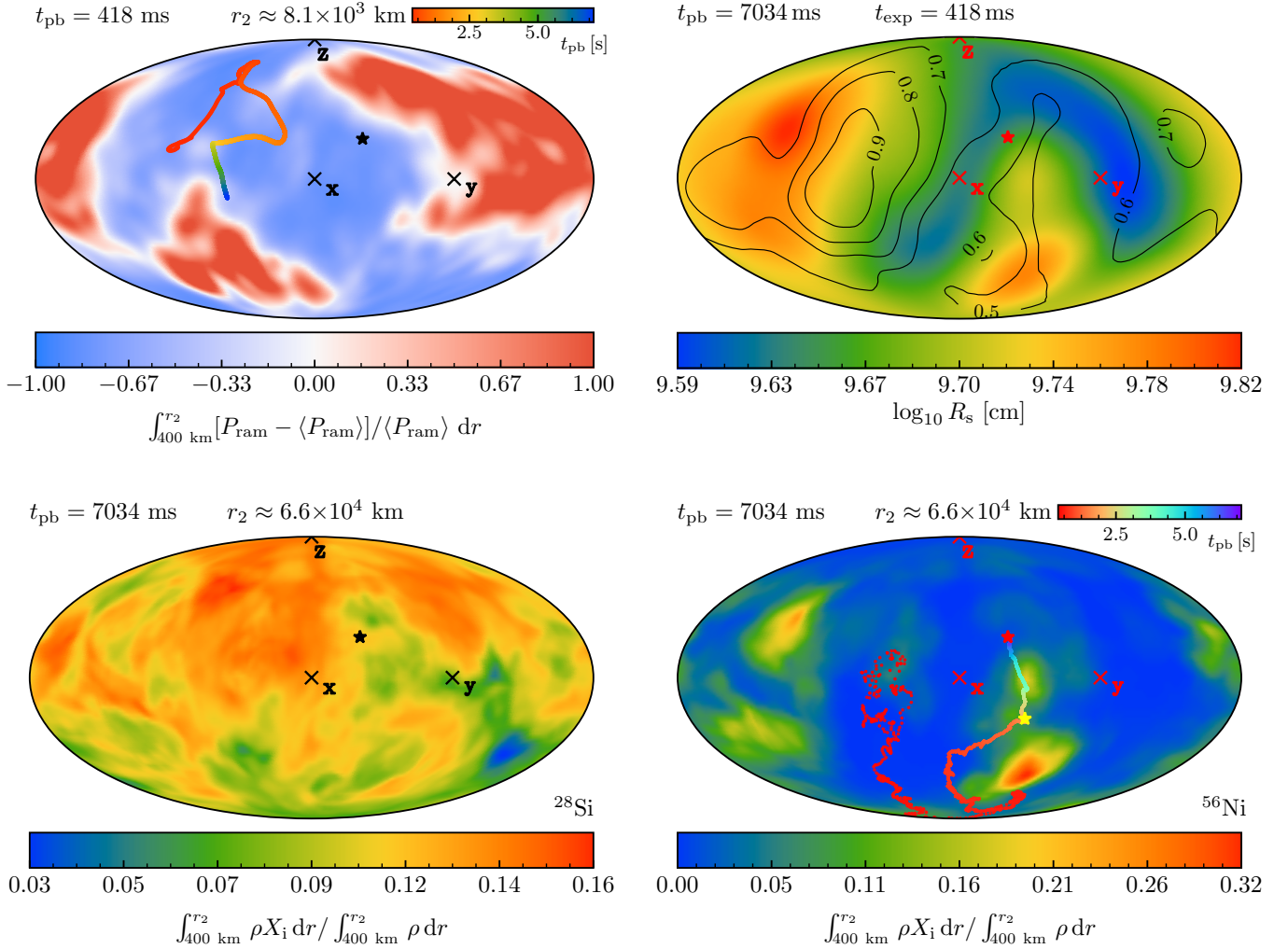


**Figure 5.** Mollweide projections of different quantities of model M\_P3D\_LS220\_m- and its extension M\_P3D\_LS220\_m-HC. In all panels the  $x$ ,  $y$ , and  $z$  directions of the coordinate axes shown in Figures 3, 4, and 9 are indicated for enabling 3D orientation. *Top left:* Ram-pressure variations associated with large-scale asymmetries from convective O-shell burning in the 3D progenitor model, radially integrated from 400 km to 8,100 km at 0.418 s after bounce. These variations determine the development of the anisotropic SN explosion because the shock expansion is faster in low-resistance “cavities”. The marked path describes the movement of the dipole direction of the deformed shock with time (color coded along the path). It stays within the cavity in the left hemisphere. *Top right:* Shock-deformation contours around the onset of the explosion at 0.418 s after bounce (black lines corresponding to 0.6, 0.7, 0.8, and 0.9 times the maximum shock radius) overlaid on the shock surface at 7.034 s (color-coded). At the latter time the shock has a bipolar shape with a considerable dipole asymmetry (see also Figures 3 and 4). *Bottom:* Line-of-sight averages of the mass fractions of  $^{28}\text{Si}$  (*left*) and  $^{56}\text{Ni}$  (*right*) at 7.034 s after bounce, averaged between 400 km and 6,600 km. Black or red asterisks in the panels mark the direction of the total (hydrodynamic plus neutrino-induced) PNS kick at 7.034 s (different colors of the asterisks were chosen for better visibility against the colored backgrounds). The path indicated by colored dots describes the migration of the PNS kick direction with time, with the yellow asterisk marking its direction at 1.675 s, when the VERTEX neutrino transport is switched off and only the further acceleration of the PNS by the gravitational tug-boat effect is tracked later on.

cases of H\_P1D\_LS220\_m- and H\_P3D\_LS220\_m-, which are based on the 1D and 3D progenitor data, respectively, are added for comparison of the evolution prior to the onset of the SN explosion.

External forcing by infalling O-shell perturbations acts as an additional driver of large-scale, nonradial fluid motions (convective overturn or SASI) in the postshock

layer besides neutrino heating and thus supports shock revival. This can be quantified by an increase of efficiency factors for the conversion of neutrino heating to turbulent kinetic energy, defined as

$$\eta_{\text{conv},i} = \frac{E_{\text{kin},i}/M_g}{[(R_s - R_g)(\dot{Q}_\nu/M_g)]^{2/3}} \quad (1)$$

(Müller & Janka 2015; Müller et al. 2017a), where  $i$  denotes radial ( $r$ ) or nonradial ( $\theta$  plus  $\phi$ ) motions. The  $E_{\text{kin},i}$  are the corresponding turbulent kinetic energies (equations (10) and (11) in Müller et al. 2017a),  $M_g$  is the mass in the gain layer,  $R_s$  and  $R_g$  angular averages of shock radius and gain radius, respectively, and  $\dot{Q}_\nu$  the integrated neutrino-heating rate in the gain layer. Between  $t_{\text{pb}} \approx 200$  ms until shortly after the explosion begins at  $t_{\text{pb}} \approx 400$  ms, we find efficiency factors between 0.3 and 0.4, in rough agreement with values obtained in SN simulations with a 3D progenitor by Müller et al. (2017a).

The large-scale density variations in the infalling O-shell trigger a highly asymmetric explosion (Figures 3 and 4) with the shock expanding faster in directions of lower ram pressure (Figure 5). The biggest expanding bubble is located close to the negative  $y$ -direction, and although the shock dipole vector drifts considerably during the first second and finds a stable position only after a few seconds, the deformation of the shock remains stable during the whole simulation, characterized by a huge outward bulge in the negative  $y$ -hemisphere (close to the dipole direction) and a second big plume between the positive  $y$ -axis and negative  $z$ -axis (Figure 5). Since the low-resolution model L\_P3D\_LS220\_m- was started from the same asymmetric 3D progenitor conditions, the most prominent plume driving the shock expansion develops also in the negative  $y$ -direction of this model (see Figure A2 in Appendix A). However, a second, smaller plume grows between the positive  $y$ -axis and positive  $z$ -axis, which lies in the periphery of the wide ram-pressure “depression” extending around the positive  $x$ -direction in the upper left panel of Figure 5, just as the secondary plume does in model M\_P3D\_LS220\_m-.

### 3.3. Explosion energy

The blast-wave energy increases continuously from the onset of the explosion until several seconds later. The diagnostic energy,  $E_{\text{exp}}^{\text{diag}}$  (which is the integrated internal plus gravitational plus kinetic energy of all postshock matter with a positive value of this total energy), effectively saturates at  $\sim 5$ s, whereas the explosion energy that accounts for the negative binding energy of overlying stellar layers (“overburden”, OB),  $E_{\text{exp}}^{\text{OB-}}$ , rises further to nearly converge to the diagnostic energy at a value around 0.98 B at 7.035 s (Figure 2). During all this time, a “classical” spherically symmetric neutrino-driven wind does not develop, but the PNS environment displays turbulent mass flows, because accretion down-drafts carry matter to locations near the gain radius ( $R_g$ ), where the gas absorbs energy from neutrino heating before it returns back outward to enhance the power of the explosion (Figure 4). The entropy per baryon in the outflows stays moderately high ( $s \sim 20\text{--}45$  k<sub>B</sub> per nucleon) and  $Y_e$  very close to 0.5.

As described by Marek & Janka (2009) and quantified by Müller (2015) and Müller et al. (2017a), the mass out-

flow rate,  $\dot{M}_{\text{out}}$  (for  $v_r > 0$ ), is determined by neutrino energy deposition, which provides the energy to gravitationally unbind the matter carried to the vicinity of the PNS in downflows, whereas the long-time growth of the explosion energy is mainly fueled by the subsequent recombination energy of free nucleons re-assembling into  $\alpha$ -particles and heavy nuclei when the downflow material expands back outward. The net effect is captured by relations for the outgoing energy and enthalpy fluxes (Figure 2):

$$F_{e,\text{out}} = \dot{M}_{\text{out}} \bar{e}_{\text{out}} = \dot{E}_{\text{exp}}^{\text{diag}} \approx 0.5 \dot{Q}_\nu, \quad (2)$$

confirming results in Müller et al. (2017a), and

$$F_{h,\text{out}} = \dot{M}_{\text{out}} \bar{h}_{\text{out}} = \dot{E}_{\text{exp}}^{\text{OB-}} \approx \dot{Q}_\nu. \quad (3)$$

Here,  $\dot{M}_{\text{out}}$ ,  $F_{e,\text{out}}$ , and  $F_{h,\text{out}}$  are defined as in equations (5), (6), and (7) of Müller (2015),  $\bar{e}_{\text{out}}$  and  $\bar{h}_{\text{out}}$  are the total energy and enthalpy per baryon (including gravitational energy) in outflows, and all of these quantities are evaluated at 400 km. These relations express energy conservation during the buildup of the explosion energy. The latter is provided by neutrino energy deposition, which does not only account for the growth of the positive energy transported by neutrino-heated ejecta ( $\dot{E}_{\text{exp}}^{\text{diag}}$  in Equation (2)) but also for the energy that is needed to gravitationally unbind the stellar layers that are swept up by the propagating shock, an effect that is included in  $\dot{E}_{\text{exp}}^{\text{OB-}}$  in Equation (3). At  $t_{\text{pb}} \lesssim 2$  s one can find time intervals when  $\dot{Q}_\nu$  exceeds  $F_{h,\text{out}} \sim \dot{E}_{\text{exp}}^{\text{OB-}}$ . This indicates that some neutrino energy is deposited in downflows instead of outflows, and subsequently this energy gets lost again by the re-emission of neutrinos around the (non-spherical) gain radius. Therefore the heating mechanism is not perfectly efficient to feed energy into the explosion.

Neutrinos thus power the explosion and there is no major net gain of energy from nuclear dissociation in downflows and later recombination in outflows as pointed out by Marek & Janka (2009): Matter from the Si-, O-, and Ne-shells gets disintegrated during infall, stores the nuclear binding energy transiently in free nucleons, which release it again when they recombine to iron-group nuclei and  $\alpha$ -particles during re-ejection. The net gain of energy this way is  $\lesssim (0.5\text{--}1)$  MeV/nucleon, and therefore the net energy carried on average per outflowing nucleon, which is  $\bar{h}_{\text{out}} \sim (3\text{--}11)$  MeV or  $\bar{e}_{\text{out}} \sim (1.5\text{--}7.5)$  MeV (Figure 2), is provided by neutrino absorption.

These energies exhibit decreasing trends with time because at early times the downflows reach or penetrate  $R_g$ , whereas at later times they return outward from larger radii because of turbulent and shear interaction with outflows. Müller et al. (2017a) demonstrated this by tracer particles. Instead, we compute an average turnaround radius,  $R_{\text{ret}}$ , from the condition that

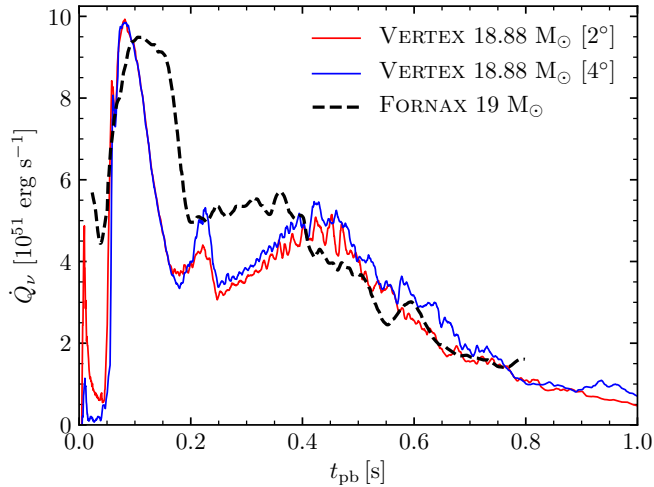


**Figure 6.** Net neutrino energy deposition rate in the gain layer as function of time,  $\dot{Q}_\nu(t)$ , for our models M\_P3D\_LS220\_m- (with  $2^\circ$  angular resolution) and L\_P3D\_LS220\_m- ( $4^\circ$  angular resolution) compared to the  $19M_\odot$  SN calculation with the FORNAX code by Burrows et al. (2020), see their Figure 5. The data from our PROMETHEUS-VERTEX simulations are smoothed with a running window of 5ms and are plotted only until 1s post bounce for good comparison; the later evolution for model M\_P3D\_LS220\_m- and its extension M\_P3D\_LS220\_m-HC is depicted in the upper right panel of Figure 2. The considerable differences between PROMETHEUS-VERTEX and FORNAX results between  $\sim 0.1$ s and  $\sim 0.4$ s are probably connected to the fact that the SN shock contracts after a local maximum at  $\sim 0.07$ s in our models (see Figure A1), whereas it expands continuously in the FORNAX simulation (see Figure 2 in Burrows et al. 2020), which leads to a larger mass in the gain layer and therefore a higher net neutrino energy deposition rate.

neutrino-heating drives the outflows, i.e.:

$$\eta_{\text{out}} = \frac{\dot{M}_{\text{out}}(R_{\text{ret}}) |e_{\text{tot}}(R_{\text{ret}})|}{\dot{Q}_\nu} = 1. \quad (4)$$

With equally good motivation this equation could be evaluated with the total enthalpy per nucleon,  $|h_{\text{tot}}(R_{\text{ret}})|$ , instead of  $|e_{\text{tot}}(R_{\text{ret}})|$ , but this would only lead to a small (outward) shift of  $R_{\text{ret}}$ , because the gravitational binding energy typically dominates. Figure 2 shows that  $R_{\text{ret}}$  is initially around 30 km but at  $t_{\text{pb}} \gtrsim 3$ s grows to  $\sim 100$  km, with no clear dependence on  $2^\circ$  or  $4^\circ$  resolution until  $\sim 2$ s. The ratio  $\alpha = \dot{M}_{\text{out}}(400 \text{ km})/\dot{M}_{\text{out}}(R_{\text{ret}})$  is typically between 1 and 2, but fluctuates stochastically to reach  $\sim 10$  in peaks, signalling that a large fraction of the infalling matter returns outward from  $r > R_{\text{ret}} \gg R_g \lesssim 30$  km. At 400 km and  $t_{\text{pb}} \gtrsim 0.8$ s we measure mass-inflow ( $v_r < 0$ ) and outflow ( $v_r > 0$ ) rates roughly in balance,

i.e.,  $\dot{M}_{\text{in}} \approx \dot{M}_{\text{out}}$  (Figure 2), and consequently the PNS baryonic mass of  $1.865 M_\odot$  becomes effectively constant (Figure 10; Table 1), corresponding to a gravitational mass of  $1.675 M_\odot$  at 7s after bounce.

Burrows et al. (2020) have recently published a large set of 3D models, exploding and non-exploding, which might partly also develop sizable explosion energies. However, all of these simulations were terminated well before 1s after bounce at a stage when the diagnostic explosion energy had just started to grow. Their most energetic model, a  $19 M_\odot$  case, has reached between 0.2B and 0.3B at the end of their computations at 0.8–0.87s (depending on the employed resolution). This model is also the most suitable one for a comparison with M\_P3D\_LS220\_m-, although a detailed assessment is hampered by the fact that the progenitors are not the same. Despite a slightly smaller PNS mass and the correspondingly lower neutrino luminosities in the simulation by Burrows et al. (2020), the neutrino heating rate as plotted in their Figure 5 is fairly similar to our model at  $t_{\text{pb}} \gtrsim 0.4$ s (see Figure 6).<sup>3</sup> In line with this finding, the diagnostic explosion energy and its growth rate at 0.87s are also quite close to our model.<sup>4</sup> Similarly, although the shock expansion sets in earlier and without a transient phase of contraction in the simulation of Burrows et al. (2020), and although the diagnostic explosion energy rises correspondingly earlier, the shock radius and shock velocity are again compatible with those in our model M\_P3D\_LS220\_m- at the time when Burrows et al. (2020) stopped their calculation.

Based on a large set of 2D simulations, Nakamura et al. (2015) explored systematic features of axisymmetric neutrino-driven SN models. They concluded that the accretion luminosity becomes higher for progenitor stars with high core-compactness parameter (O’Connor & Ott 2011), because the latter correlates with the density of the shells surrounding the degenerate iron core. Nakamura et al. (2015) further argued that the higher accretion luminosity leads to a higher growth rate of the diagnostic energy and of the synthe-

<sup>3</sup> We point out that the net neutrino heating rate is considerably higher than the growth rate of the diagnostic explosion energy,  $\dot{E}_{\text{exp}}^{\text{diag}}$ , plotted in Figure 2, because most of the deposited energy is used up to gravitationally unbind the expelled matter, i.e., to overcome its gravitational binding energy. Moreover, we remark that the neutrino energy deposition rate during the first second after bounce dwarfs by far estimates of the heating in the postshock layer due to the energy flux carried by gravity waves and outgoing acoustic waves. Such waves can be excited by PNS convection and their energy and its fraction potentially transmitted upwards to the postshock region have recently been estimated on grounds of 1D simulations by Gossan et al. (2020).

<sup>4</sup> It should be noted, however, that the diagnostic explosion energies plotted in Figure 6 of Burrows et al. (2020) differ in their definition from our use of  $E_{\text{exp}}^{\text{diag}}$ . The diagnostic explosion energies given by Burrows et al. (2020) include ‘reassociation energy’ and gravitational binding energy of matter exterior to the shock, whereas our diagnostic explosion energies do not.

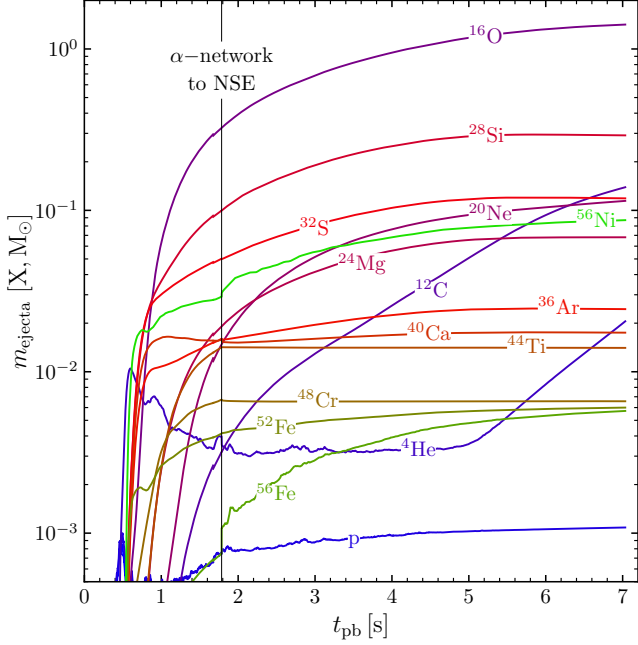


**Figure 7.** Ejecta masses of chemical species in the post-shock volume of model M.P3D\_LS220\_m– and its extension M.P3D\_LS220\_m–HC. The vertical line marks the moment when the  $\alpha$ -network was replaced by an NSE treatment applied above  $T = 0.343$  MeV.

sized nickel mass. While we agree that there is a close correlation between the rate of mass-infall towards the PNS and the core compactness of the progenitor, we emphasize that the long-time growth of the explosion energy and nickel yield in our 3D model is *not* connected to a higher accretion luminosity. As mentioned above, the PNS stops accreting at about 0.8 s after bounce. Instead, the long-time growth of the explosion energy is fueled by the efficient neutrino heating of the infalling flows of gas, which absorb energy from neutrinos and then return outward. At  $t_{\text{pb}} \gtrsim 0.8$  s the mass inflow and outflow rates have become effectively equal, and the subsequent steep rise of the explosion energy is a consequence of the long-lasting high mass-infall rate (which is correlated with the core compactness) on the one hand, and the efficient neutrino heating due to high PNS cooling luminosities, which blows the infalling matter out again, on the other hand. The process of reversing inflow to outflow is significantly more efficient in 3D models than in the case of axi-symmetric geometry (as discussed in detail by Müller 2015; Müller et al. 2017a, 2019).

### 3.4. Nucleosynthesis yields

Radioactive  $^{56}\text{Ni}$  and other elements heavier than  $^{28}\text{Si}$  are produced either by explosive burning or normal and alpha-rich freeze-out (see, e.g., Hix & Thielemann 1999b; Magkotsios et al. 2010). They are ejected

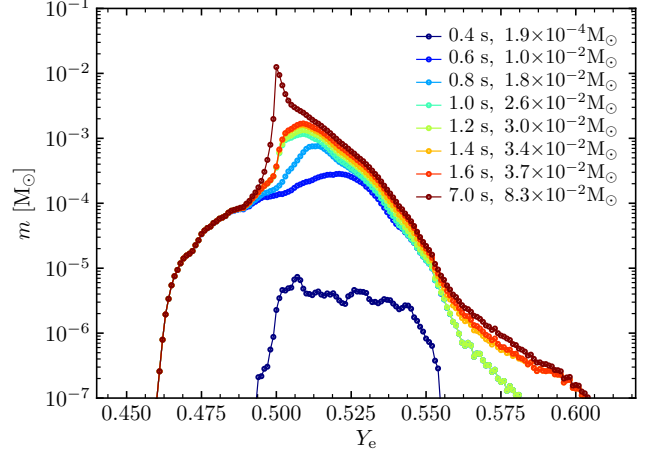


**Figure 8.** Mass distributions versus electron fraction  $Y_e$  of neutrino-heated ejecta at different post-bounce times for model M.P3D\_LS220\_m– and its extension M.P3D\_LS220\_m–HC. The distributions were constructed from all ejecta flowing out through a sphere of 250 km radius.

in the highest concentrations in regions where the shock is strongest (Figure 5), in agreement with findings of Wongwathanarat et al. (2013), whereas such a correlation is effectively lost for  $^{28}\text{Si}$  and lighter elements (Figure 5). Using the small network we obtain ejecta masses of  $0.29 M_{\odot}$  of silicon and  $1.42 M_{\odot}$  of oxygen. A mass of  $0.028 M_{\odot}$  of  $^{56}\text{Ni}$  is nucleosynthesized during the PROMETHEUS-VERTEX run of model M.P3D\_LS220\_m– until  $\sim 1.7$  s, increasing to an upper estimate of  $\lesssim 0.087 M_{\odot}$  until  $\sim 7$  s during the continuation by model M.P3D\_LS220\_m–HC (Figure 7). Efficient formation of  $^{56}\text{Ni}$  under conditions of alpha-rich freeze-out is enabled because the electron fraction,  $Y_e$ , of most of the neutrino-processed ejecta varies between  $\sim 0.495$  and  $\sim 0.52$  (Figures 8 and 9). Since the extended run was done with an NSE solver applied down to lower temperatures instead of the network, the  $^{56}\text{Ni}$  production may be overestimated, as suggested by the discontinuous growth rate of the  $^{56}\text{Ni}$  mass after the network-NSE switch (Figure 7). Our final  $^{56}\text{Ni}$  mass is therefore an upper limit, and we expect the actual mass to be around  $0.05 M_{\odot}$  (see below). Nevertheless, values in this range demonstrate that  $^{56}\text{Ni}$  masses close to those of typical CCSNe can be ejected in 3D neutrino-driven explosions. The continuous growth of the ejected masses of intermediate-mass elements displayed in Figure 7 mostly reflects the composition of the stellar shells swept up by the outgoing shock.

Interestingly, the mass-versus- $Y_e$ -distribution of the neutrino heated-ejecta in our simulation of M.P3D\_LS220\_m– and its extension M.P3D\_LS220\_m–HC (Figure 8; see also Figure A3 for the corresponding result of our  $4^{\circ}$ -model L.P3D\_LS220\_m–), is perfectly compatible with important nucleosynthetic constraints discussed by Hoffman

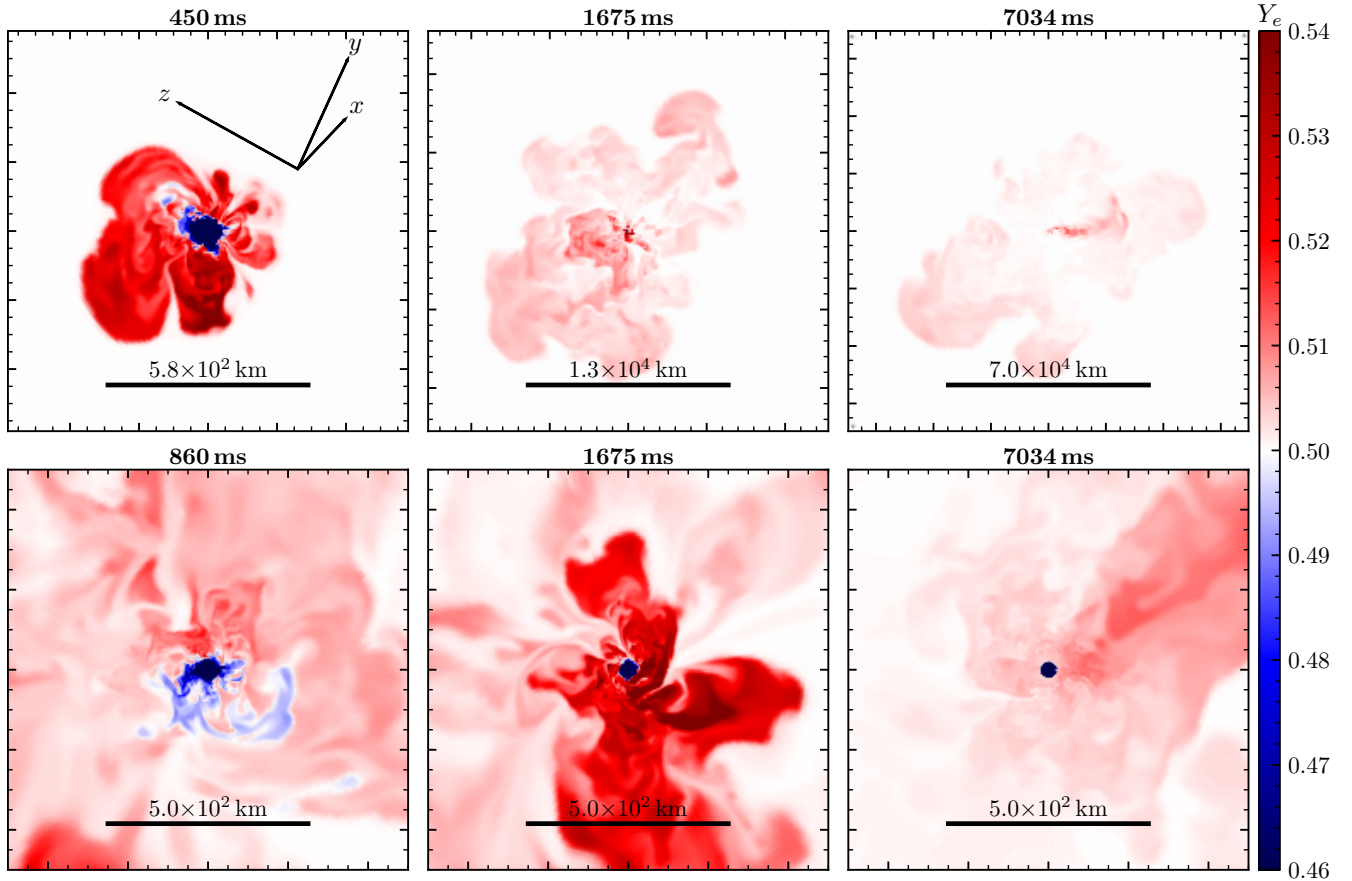


**Figure 9.** Electron fraction in the outflows of model `M_P3D_LS220_m-` and its extension `M_P3D_LS220_m-HC`. The cross-sectional plane is the same as the one chosen in Figure 4. *Top:*  $Y_e$  color-coded at 0.450 s, 1.675 s, and 7.034 s matching the times in Figure 4. *Bottom:* Close-ups of the turbulent vicinity of the PNS at 0.86 s, 1.675 s, and 7.034 s after bounce.  $Y_e$  in the ejecta is close to or slightly larger than 0.50.

et al. (1996). According to these authors, typical Type-II SNe should eject  $\lesssim 10^{-4} M_\odot$  of neutrino-heated matter with  $Y_e \lesssim 0.47$  in order not to overproduce  $N = 50$  closed neutron shell nuclei. This approximate limit is fulfilled by the  $2^\circ$  model as well as the  $4^\circ$  explosion model (see also Appendix A).

The use of a small  $\alpha$ -network in the PROMETHEUS-VERTEX run does not permit accurate predictions of the nucleosynthetic yields. For example, it overestimates the production of  $^{44}\text{Ti}$  by up to a factor of 100 (see also Wongwathanarat et al. 2013). Large-network calculations in a post-processing analysis will have to clarify whether most of this  $^{44}\text{Ti}$  as well as some fraction of  $^{48}\text{Cr}$  might rather end up as iron and  $^{56}\text{Ni}$ , as it happens when we replace the network by the NSE solver.

Most important in the present context, however, is the fact that in neutrino-driven explosions there is a tight correlation between the mass ejected in neutrino-heated freeze-out material,  $M_{\text{ej}}^{\text{fo}}$ , and the diagnostic explosion energy,  $E_{\text{exp}}^{\text{diag}}$ . Since on average each ejected nucleon contributes a net energy of  $\bar{\epsilon}_{\text{out}} \sim 5$  MeV to the explosion

energy (Janka 2001; Scheck et al. 2006; Marek & Janka 2009; Müller 2015, see also Section 3.3), about  $0.1 M_\odot$  of neutrino-heated matter must be expelled to power a SN that blows up with an energy of 1 B:<sup>5</sup>

$$E_{\text{exp}}^{\text{diag}} \approx 1 \text{ B} \times \left( \frac{\bar{\epsilon}_{\text{out}}}{5 \text{ MeV/nucleon}} \right) \times \left( \frac{M_{\text{ej}}^{\text{fo}}}{0.1 M_\odot} \right). \quad (5)$$

We can thus, very crudely, bracket the likely yield of  $^{56}\text{Ni}$  by the following arguments. At 1.7 s our small network has produced  $0.028 M_\odot$  of  $^{56}\text{Ni}$ . At this time

<sup>5</sup> The diagnostic explosion energy of model `L_P3D_LS220_m-` is approximately 0.63 B at 1.884 s after bounce (Table 1), which is  $\sim 0.12$  B higher than in model `M_P3D_LS220_m-` at roughly the same time. This is fully compatible with the estimate of Equation (5), because the baryonic mass of the PNS in model `L_P3D_LS220_m-` at this instant is  $\sim 1.2 \times 10^{-2} M_\odot$  lower than in model `M_P3D_LS220_m-`, which suggests a slightly lower accretion efficiency and a correspondingly larger rate of mass outflow. The increased ejecta mass carries the additional supply of explosion energy, because it has absorbed extra energy deposited by neutrinos near the gain radius or turnaround radius.

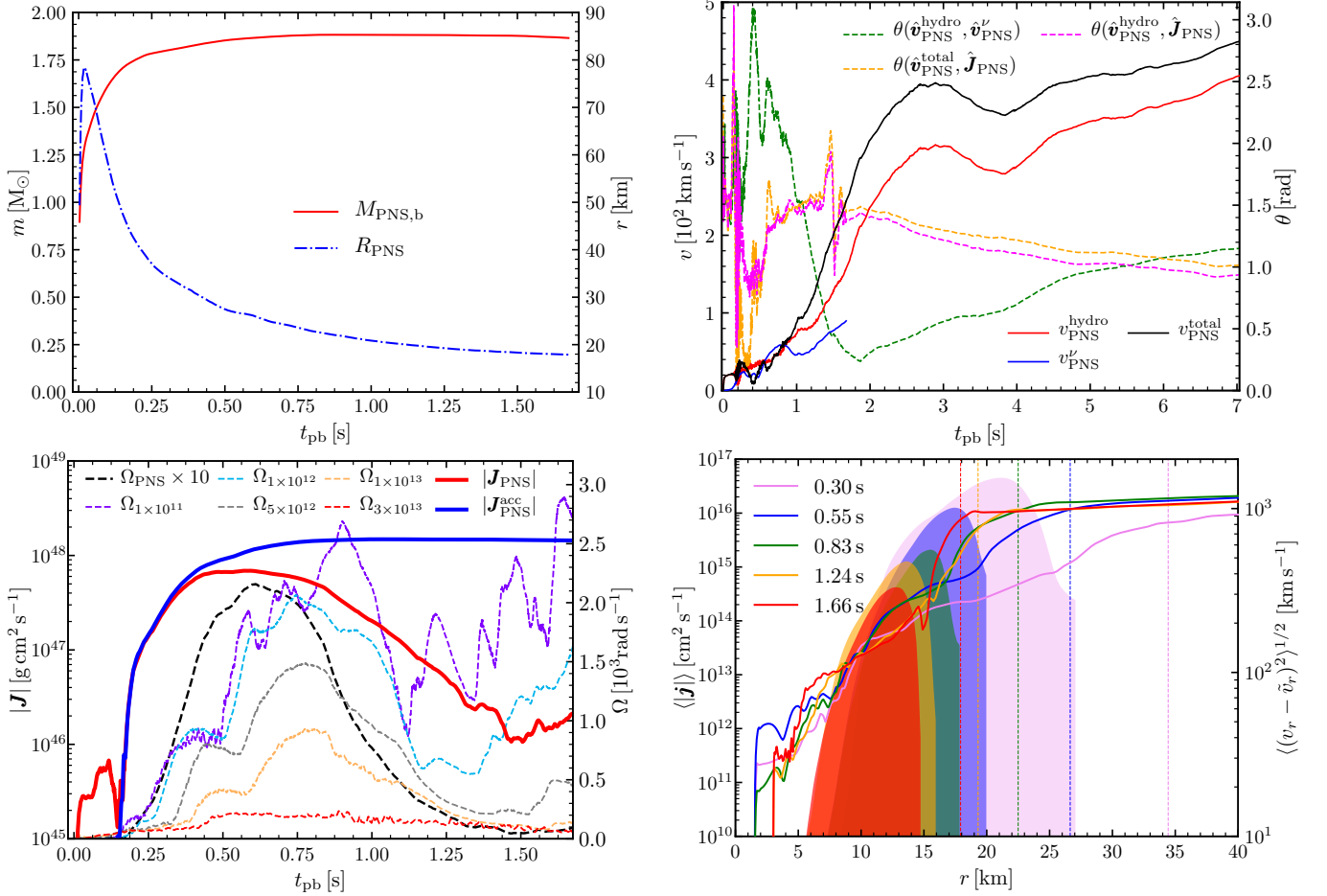


**Figure 10.** Proto-neutron star (PNS) properties of model `M_P3D_LS220_m-` during the simulation with VERTEX neutrino transport. The top right panel also shows data from the extended calculation of `M_P3D_LS220_m-HC` with heating and cooling treatment instead of VERTEX transport. *Top left:* Baryonic mass and radius, both corresponding to the volume where the mass-density  $\rho \geq 10^{11} \text{ g cm}^{-3}$ . *Top right:* Neutrino-induced kick velocity ( $v_{\text{PNS}}^{\nu}$ ), hydrodynamic kick ( $v_{\text{PNS}}^{\text{hydro}}$ ), and sum of both (total kick,  $v_{\text{PNS}}^{\text{total}}$ ) and relative angles between hydrodynamic and neutrino-induced kick velocities, hydrodynamic kick and PNS angular momentum vector, and total kick and PNS angular momentum vector. The evolution of hydrodynamic and total kick can be tracked also after the end of the VERTEX calculation, the neutrino-induced kick and the PNS spin direction are unchanged after 1.675 s post bounce. *Bottom left:* Net accretion of angular momentum onto the PNS ( $|\mathbf{J}_{\text{PNS}}^{\text{acc}}|$ ), total PNS angular momentum (for  $\rho \geq 10^{11} \text{ g cm}^{-3}$ ;  $|\mathbf{J}_{\text{PNS}}|$ ), average angular velocity  $\Omega_{\text{PNS}}$  if the PNS were rigidly rotating with  $|\mathbf{J}_{\text{PNS}}|$ , and angular velocities  $\Omega_{\rho}$ , averaged over isosurfaces of density  $\rho$  for the values given as subscripts (in  $\text{g cm}^{-3}$ ). *Bottom right:* Radial profiles of the angle-averaged (with density-weighting) specific angular momentum at different post-bounce times (colored lines). The corresponding colored areas show angle-averaged radial turbulent velocities, indicating the convective layer inside the PNS. The thin vertical dashed lines mark the radii where the average density is  $10^{11} \text{ g cm}^{-3}$ . It is obvious that the PNS rotation is highly differential, the specific angular momentum is highest in the convectively stable outer PNS layers, and inward transport of angular momentum by PNS convection is not efficient.

the diagnostic explosion energy has just reached half of its final value. The rest of the explosion energy is provided by continuous neutrino heating of matter that falls inward with a fairly high rate for seconds and gets re-ejected with  $\dot{M}_{\text{out}} \approx |\dot{M}_{\text{in}}|$  after having absorbed energy from neutrinos (Figure 2). Since the energy or enthalpy per ejected nucleon are nearly constant until about 5 s, about the same mass of neutrino-heated matter shares the explosion energy before and after 1.7 s. Assuming

the same efficiency for the recombination of neutrino-heated ejecta to  $^{56}\text{Ni}$  before and after 1.7 s, an optimistic total yield of  $^{56}\text{Ni}$  can be estimated roughly as  $2 \times 0.028 M_{\odot} = 0.056 M_{\odot}$ .

However, some of the very early production of  $^{56}\text{Ni}$  might have been made by explosive burning in the shock-heated ejecta, which takes place only for a few hundred milliseconds and could account for the steep rise of the ejected  $^{56}\text{Ni}$  to a short plateau of  $\sim 0.018 M_{\odot}$  at

about 1 s (see Figure 7). Assuming that none of this early  $^{56}\text{Ni}$  comes from freeze-out (which is an unlikely, pessimistic case), freeze-out until 1.7 s would only contribute  $0.01 M_{\odot}$  of the  $^{56}\text{Ni}$  made until that time by our small network. Again assuming the same freeze-out production of  $^{56}\text{Ni}$  before and after 1.7 s, we thus derive a pessimistic lower estimate of the total yield as  $0.028 M_{\odot} + 0.01 M_{\odot} = 0.038 M_{\odot}$ .

The actual number is probably somewhere between  $0.038 M_{\odot}$  and  $0.056 M_{\odot}$ . Since some of the  $^{44}\text{Ti}$ ,  $^{48}\text{Cr}$ , and  $^{52}\text{Fe}$  might well be  $^{56}\text{Ni}$  instead, we tend to favor a value towards the optimistic side and consider  $\sim 0.05 M_{\odot}$  as a reasonable, though crude, estimate of the total nucleosynthesized  $^{56}\text{Ni}$  mass. This would be well compatible with the yield of SN 1987A, whose explosion energy and  $^{56}\text{Ni}$  ejecta have been determined from light-curve analysis to be about 1.5 B and  $0.0765 M_{\odot}$ , respectively (Utrobin & Chugai 2011, and references therein). We therefore think there are no reasons to postulate a “nickel mass problem” connected to the slow increase of the explosion energy in neutrino-driven SN blasts (Suwa et al. 2019; Sawada & Suwa 2021). It is obvious from our 3D simulations that neutrino-driven explosions eject sufficient freeze-out material to account for the observed  $^{56}\text{Ni}$  masses in Type-II SNe. Detailed nucleosynthesis calculations will have to reveal the exact fraction of this radioactive species in the neutrino-heated ejecta.

### 3.5. Proto-neutron star properties

#### 3.5.1. Proto-neutron star spin

At  $t_{\text{pb}} \lesssim 0.9$  s downflows emanating from the convectively perturbed O-shell (with specific angular momentum up to  $j > 10^{16} \text{ cm}^2 \text{ s}^{-1}$ ) carry considerable angular momentum ( $\sim 1.5 \times 10^{48}$  ergs; Figure 10) toward the PNS. Some of this high- $j$  matter ( $\sim 50$ – $60\%$  at  $t_{\text{pb}} \lesssim 0.9$  s) is blown out again by neutrino heating, but its partial accretion spins up the outer PNS layers at densities  $\rho \lesssim 10^{13} \text{ g cm}^{-3}$  with a dominant negative  $y$ -component, which is  $\sim 3$  times greater than the  $x$ - and  $z$ -components. In peaks the angular velocity reaches  $(2\text{--}3) \times 10^3 \text{ rad s}^{-1}$  at densities  $10^{11} \text{ g cm}^{-3} \lesssim \rho \lesssim 10^{12} \text{ g cm}^{-3}$  (Figure 10) and decreases inward. Only about half of the accreted angular momentum (i.e., of the excess of inflow compared to outflow of angular momentum), however, shows up in the PNS mantle at  $t_{\text{pb}} \lesssim 0.6$  s (compare the blue and red bold solid lines in the lower left panel of Figure 10). After accretion onto the PNS ends at  $t_{\text{pb}} \sim 0.8$  s, the angular momentum stored in the near-surface layers with densities between a few times  $10^{11} \text{ g cm}^{-3}$  and some  $10^{13} \text{ g cm}^{-3}$  declines quite rapidly with time. Therefore, there is a huge drain of accreted angular momentum from  $t_{\text{pb}} \sim 0.4$  s until  $t_{\text{pb}} \sim 1.3$  s, in course of which the outer PNS layers above a few  $10^{11} \text{ g cm}^{-3}$  decelerate dramatically.

We have not (yet) been able to identify the origin of this angular momentum loss unambiguously. The ef-

fect is only moderately dependent on the angular resolution. The long-time evolution of the angular momentum on the entire computational grid and in the PNS volume is qualitatively very similar and quantitatively only little different in model `M_P3D_LS220_m-` and its lower-resolution counterpart `L_P3D_LS220_m-` (compare the bottom left panel of Figure 10 with Figure B1 and see Figure B2). Despite this modest resolution dependence, we cannot exclude that the deceleration of the PNS rotation is caused by imperfect numerical conservation of angular momentum in the hydrodynamics scheme (as discussed by Müller 2020), possibly enhanced by the use of the Yin-Yang grid and the corresponding treatment of the fluxes across the grid interfaces. More information on this aspect can be found in Appendix B.

It might also be possible that the angular momentum loss from the PNS surface layers is, maybe partly, connected to the coupling of hydrodynamics and  $\text{RbR+}$  neutrino transport. This approximation includes nonradial components of the neutrino pressure gradients in the fluid equation of motion in the optically thick regime and nonradial neutrino advection with the moving medium in the transport equations (Buras et al. 2006), but it disregards effects of neutrino viscosity and nonradial neutrino flux components. Therefore it cannot handle angular momentum transport by neutrinos, but it is difficult to track down the exact consequences of the nonradial neutrino pressure derivatives for the angular momentum evolution of the background medium the neutrinos propagate through.

Interestingly, however, the growing mismatch between the angular momentum accreted onto the PNS and the angular momentum available in its near-surface layers could indeed be caused by neutrinos carrying away this difference. Angular momentum is exchanged between matter and neutrinos in layers where both are strongly coupled (i.e., at  $\rho \gtrsim$  some  $10^{11} \text{ g cm}^{-3}$ ), before the neutrinos escape more easily from lower-density regions. These low-density layers should continue to spin rapidly, which indeed is the case in Figure 10. Considering the neutrino-energy loss,  $\Delta E_{\nu}$ , during the relevant time between  $\sim 0.4$  s and  $\sim 1.3$  s after bounce, the PNS radius,  $R_{\text{PNS}}$ , and the average PNS angular velocity at  $R_{\text{PNS}}$ ,  $\bar{\Omega}_{\text{PNS}}^{\text{surf}} \sim \Omega_{1 \times 10^{11}}$ , one obtains a rough estimate for the angular momentum extracted by neutrinos as

$$\begin{aligned} \Delta J_{\nu} &= \frac{1}{c^2} \Delta E_{\nu} R_{\text{PNS}}^2 \bar{\Omega}_{\text{PNS}}^{\text{surf}} \\ &\approx 1.4 \times 10^{48} \left( \frac{\Delta E_{\nu}}{10^{53} \text{ erg}} \right) \left( \frac{R_{\text{PNS}}}{25 \text{ km}} \right)^2 \\ &\quad \left( \frac{\bar{\Omega}_{\text{PNS}}^{\text{surf}}}{2000 \text{ rad s}^{-1}} \right) \text{ erg s}. \end{aligned} \quad (6)$$

This estimate is comparable to the depletion of accreted angular momentum visible in Figure 10 between  $\sim 0.5$  s and  $\sim 1$  s. But, of course, the agreement of this estimate



with the numerical results is not a proof that the angular momentum decline in our simulations is indeed connected to the neutrino emission. The similar magnitude of the effects might also be an astounding coincidence.

In the considered situation the angular momentum is highly concentrated in near-surface layers of the PNS, which are formed by accreted matter and where neutrinos undergo their last few interactions before they begin to decouple from the stellar background (heavy-lepton neutrinos around  $\sim 10^{12} \text{ g cm}^{-3}$ ,  $\nu_e$  and  $\bar{\nu}_e$  between  $\sim 10^{12} \text{ g cm}^{-3}$  and  $\gtrsim 10^{11} \text{ g cm}^{-3}$ ). Under such conditions the escaping neutrinos can extract angular momentum extremely efficiently, thus possibly impeding the spin-up of the PNSs by SASI spiral modes (e.g., Blondin & Mezzacappa 2007; Kazeroni et al. 2017), (intermittent) accretion disk formation (e.g., Gilkis & Soker 2014), and magnetic field amplification by angular momentum accretion (Soker 2020). Disk formation around the new-born NS is a crucial ingredient of the “jittering-jet mechanism” (e.g., Papish & Soker 2011, 2014). It was suggested to be facilitated by the infall of material from the convective O-burning and He-layers, where convective motions might possess sufficient stochastic angular momentum so that the matter can assemble in orbits around the PNS (Gilkis & Soker 2014). However, not only angular momentum loss through neutrino emission (as discussed above) is a serious handicap for this scenario, but also the intense neutrino fluxes and the powerful neutrino heating in the vicinity of the PNS impede disk formation. Instead, the energy input by neutrinos reverses the infall of high-angular momentum material from the convective O-burning layer in our 3D simulations and thus strengthens the SN blast before this material could even start to accumulate in orbits around the neutrino-emitting PNS (provided it had angular momentum above the critical threshold of some  $10^{16} \text{ erg s}$  needed for disk formation). Angular momentum extraction by escaping neutrinos might be of relevance for accretion phenomena, torus formation, and disk evolution in binary NS mergers, too.

### 3.5.2. Proto-neutron star kick

Anisotropic mass ejection and neutrino emission also impart a kick to the PNS, which we evaluate along the lines described by Scheck et al. (2006); Wongwathanarat et al. (2013); Stockinger et al. (2020). Neutrinos escape from the PNS convection layer anisotropically because of the lepton-emission self-sustained asymmetry (LESA; Tamborra et al. 2014a; see also Tamborra et al. 2014b; Walk et al. 2018, 2019, 2020; O’Connor & Couch 2018; Glas et al. 2019a; Powell & Müller 2019; Vartanyan et al. 2019; Stockinger et al. 2020; Müller 2020; Nagakura et al. 2021, and references therein). This leads to a kick around  $30 \text{ km s}^{-1}$  that saturates with a dominant negative  $z$ -component at  $t_{\text{pb}} \approx 0.3 \text{ s}$ , because thereafter the LESA emission dipole gets considerably reduced, presumably by the spin-up of the outer

PNS layers (Walk et al. 2019, see also Appendix C, Figure C1). However, anisotropic neutrino emission, associated with accretion, accelerates the PNS further (now migrating between the positive  $y$ - and negative  $z$ -directions) to  $v_{\text{PNS}}^{\nu} \approx 100 \text{ km s}^{-1}$ , when evaluated at the gain radius (see again Appendix C for details). This value is asymptotically reached at  $t_{\text{pb}} \sim 0.8 \text{ s}$ , because later accretion downflows hardly penetrate through the gain radius (Figure 2; Section 3.3). Due to partial absorption of neutrinos in the gain layer, which transfers linear momentum to the SN ejecta, the relevant neutrino contribution to the total PNS kick must be evaluated in the free-streaming regime, in order to avoid that ejecta momentum received from neutrino absorption is erroneously accounted to the PNS when assuming balance between PNS and ejecta momenta. The effective neutrino-induced kick thus grows from  $v_{\text{PNS}}^{\nu} \approx 50\text{--}60 \text{ km s}^{-1}$  at  $t_{\text{pb}} \sim 0.8\text{--}1 \text{ s}$  to  $\sim 100 \text{ km s}^{-1}$  at the end of the PROMETHEUS-VERTEX run (Figure 10). The growth during this period of time is again caused by LESA, because the LESA dipole emission becomes stronger again after the rotation in the PNS near-surface layers has slowed down. This leads to a dipole component of the total neutrino luminosity (summed over all neutrino species) that persists over the entire PNS evolution simulated with the VERTEX neutrino transport, even after the mass accretion by the PNS has ended. The amplitude of the luminosity dipole amounts to about 5% of the monopole on average (see Appendix C, Figures C1 and C2). A considerable fluctuation of the direction of the luminosity dipole, however, moderates its consequences for the PNS kick.

Asymmetric mass ejection causes a much larger PNS kick, reaching  $v_{\text{PNS}}^{\text{hydro}} > 400 \text{ km s}^{-1}$  after 7 s and drifting considerably over this period of time. This yields a total kick of  $> 450 \text{ km s}^{-1}$ , because neutrino-induced and hydrodynamic kicks are in the same hemisphere (Figures 5 and 10). The total kick grows further because of the gravitational tug-boat effect. Note that  $v_{\text{PNS}}^{\text{hydro}}$  is computed as the ratio of linear momentum to the (constant) baryonic PNS mass, since  $v_{\text{PNS}}^{\text{hydro}}$  should not change in the absence of external forces when the gravitational mass of the PNS decreases due to isotropic neutrino emission in its rest frame. This expresses the fact that neutrinos radiated from a moving PNS carry linear momentum in the observer frame.

## 4. CONCLUSIONS

Model M.P3D\_LS220\_m– was evolved in 3D with the PROMETHEUS-VERTEX neutrino-hydrodynamics code continuously through the final 7 min of convective O-shell burning, core collapse, bounce, and onset of explosion at  $t_{\text{pb}} \sim 0.4 \text{ s}$  ( $\pm \sim 100 \text{ ms}$  depending on resolution and microphysics, i.e., LS220 or SFHo EoS, and muons) until  $\sim 7 \text{ s}$  after bounce. It constitutes the first case of a self-consistent 3D simulation with detailed neutrino transport that yields a neutrino-driven explosion with

properties similar to SN 1987A, namely an energy near 1 B and up to  $\sim 0.087 M_{\odot}$  of ejected  $^{56}\text{Ni}$ . Its PNS has a baryonic (gravitational) mass of  $1.865 M_{\odot}$  ( $\lesssim 1.675 M_{\odot}$ ), a kick of  $\gtrsim 450 \text{ km s}^{-1}$ , and an average (surface) spin period of roughly 600 ms (2 ms) at the end of our simulations (before fallback). Also the kick velocity is in the ballpark of values inferred for the NS in SN 1987A from measured  $^{44}\text{Ti}$ -line redshifts (Boggs et al. 2015) and detailed analyses of  $^{56}\text{Co}$ -decay,  $^{44}\text{Ti}$ -decay, and Fe infrared lines (Jerkstrand et al. 2020).

The considered non-rotating, solar-metallicity  $\sim 19 M_{\odot}$  stellar model was not constructed as a SN 1987A progenitor, but our results demonstrate the viability of the neutrino-driven mechanism to fuel powerful CCSN explosions in principle. Perturbations in the convective O-burning shell determine the asymmetry of the mass ejection, which has a pronounced bipolar structure with a large dipole component. Angular momentum associated with accretion downflows leads to time-variable spin-up of the surface layers of the PNS. Neutrinos, however, are an efficient channel of angular momentum loss because of the highly differential rotation with the largest velocities in near-surface layers where neutrinos begin to decouple.

We did not see the appearance of a spherical or quasi-spherical neutrino-driven wind in our long-time 3D simulations. Such a wind is defined as a basically isotropic outflow of matter expanding away from the PNS surface due to neutrino energy deposition. It fills the environment of the PNS and was seen as a generic feature of 1D explosion models and most parametrized multi-D explosion simulations. However, we could not witness this phenomenon in our long-time 3D explosion simulations of the  $\sim 19 M_{\odot}$  star discussed in the current paper, nor did it develop in a pure form during the first  $\sim 3$  s after the onset of the neutrino-driven explosion in a long-time 3D SN simulation of a  $9.0 M_{\odot}$  iron-core progenitor presented by Stockinger et al. (2020). Instead, accretion downflows and neutrino-heated outflows generate turbulent and highly asymmetric mass motions around the PNS until the end of the simulated evolution of NS birth and of the beginning SN explosions. In the mentioned  $9.0 M_{\odot}$  explosion the downflows become weaker and less frequent at  $\sim 3$  s after bounce, but some of them achieve to penetrate inward towards the PNS even later, because a powerful supersonic neutrino-driven wind that could provide a strong outward push does not develop.

The possibility of the wind to occur, at least for transient phases, is sensitive to the strength of the neutrino heating on the one hand, and it is likely to depend also on the rate of mass infall from the progenitor on the other hand. In fact, the long-lasting downflows ensure a continuous, abundant supply of matter that can be efficiently heated by neutrinos in the close vicinity of the PNS, taking up the energy that feeds the blast-wave until its energy approaches the terminal value several seconds after core bounce. The presence of these

long-lasting downflows is a prerequisite for powerful explosions by the neutrino-heating mechanism as in the  $\sim 19 M_{\odot}$  SN model reported here. Therefore “classical” neutrino-driven winds do not seem to be a general feature in 3D explosion simulations, at least not in cases where strong explosions with energies of more than (0.1–0.2) B (which is the power-limit of neutrino-driven winds) are obtained. Instead, isotropic neutrino-driven winds might be a phenomenon that occurs predominantly in progenitors with very low core compactness near the low-mass end of the SN range. In such progenitors the explosion develops quickly, accretion downflows and outflows cease soon after shock revival, and the blast-wave energy remains correspondingly low (see two of the three 3D simulations of low-mass SNe in Stockinger et al. 2020).

*Software:* PROMETHEUS-VERTEX (Fryxell et al. 1991; Müller et al. 1991; Rampp & Janka 2002; Buras et al. 2006), VisIt (Childs et al. 2012).

*Data availability:* Data of the initial 1D and 3D models, selected output times of the 3D SN runs, and of neutrino signals will be made available upon request in our Core-Collapse Supernova Data Archive <https://wwwmpa.mpa-garching.mpg.de/ccsnarchive/>.

We thank Henk Spruit for useful discussions and Jeanette Plechinger for her internship work on the 3D data visualization. At Garching, funding by the European Research Council through Grant ERC-AdG No. 341157-COCO2CASA and by the Deutsche Forschungsgemeinschaft (DFG, German Research Foundation) through Sonderforschungsbereich (Collaborative Research Centre) SFB-1258 “Neutrinos and Dark Matter in Astro- and Particle Physics (NDM)” and under Germany’s Excellence Strategy through Cluster of Excellence ORIGINS (EXC-2094)—390783311 is acknowledged. This work was also supported by the Australian Research Council through ARC Future Fellowship FT160100035 (BM) and Future Fellowship FT120100363 (AH), by the Australian Research Council Centre of Excellence for Gravitational Wave Discovery (OzGrav), through project number CE170100004 (BM, AH); by the Australian Research Council Centre of Excellence for All Sky Astrophysics in 3 Dimensions (ASTRO 3D), through project number CE170100013 (AH), and by the National Science Foundation under Grant No. PHY-1430152 (JINA Center for the Evolution of the Elements; AH). The authors are grateful to the Gauss Centre for Supercomputing e.V. (GCS; [www.gauss-centre.eu](http://www.gauss-centre.eu)) for computing time on the GCS Supercomputers SuperMUC and SuperMUC-NG at Leibniz Supercomputing Centre (LRZ; [www.lrz.de](http://www.lrz.de)) under GAUSS Call 17 project ID: pr53yi and GAUSS Call 20 project ID: pr53yi, and to the LRZ under LRZ project ID: pn69ho. They also thank the Max Planck Computing and Data Facility (MPCDF) for computer

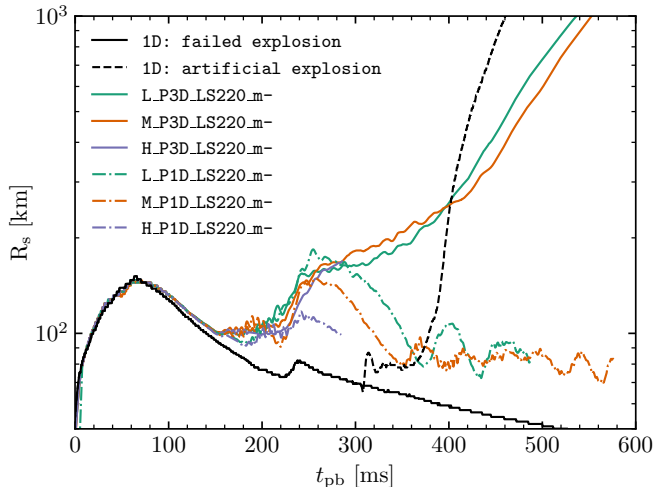


**Figure A1.** Average shock radii for all models with LS220 EoS and without muon physics. Colored solid lines correspond to the 3D models with different angular resolution (L, M, and H) employing 3D pre-collapse progenitor data. The colored dash-dotted lines display results for the corresponding cases starting from the 1D progenitor data. The black lines show the 1D simulation (solid) and the 1D model with artificially triggered explosion (dashed), whose neutrino luminosities and mean energies of the PNS are employed in the 3D extension run M.P3D.LS220\_m-HC of model M.P3D.LS220\_m-. In M.P3D.LS220\_m-HC the neutrino treatment with the VERTEX code is replaced by a heating and cooling description that requires input from the 1D PNS cooling simulation.

resources on the HPC systems Cobra and Draco. Parts of this research were undertaken with the assistance of resources and services from the National Computational Infrastructure (NCI), which is supported by the Australian Government. They were also facilitated by resources provided by the Pawsey Supercomputing Centre with funding from the Australian Government and the Government of Western Australia.

## APPENDIX

### A. ADDITIONAL INFORMATION FOR MODEL SUBSET WITH LS220 EOS AND NO MUONS

For comparison with model M.P3D.LS220\_m- (and its extension M.P3D.LS220\_m-HC), which we focus our discussion on in the main text, we present in this appendix a few selected results for a subset of the other cases listed in Table 1. All of these considered models have been computed with the LS220 EoS and without muons, but possess different angular resolutions and are either based on the 1D or 3D progenitor data.

Figure A1 displays the average shock radii of the L, M, and H models both for the runs started from the 1D progenitor and from the 3D initial conditions. All three 3D

core-collapse simulations initiated with the 1D data do not exhibit an evolution towards explosion, whereas the three models based on the 3D progenitor data develop explosions. The high-resolution case H.P3D.LS220\_m- is not finally conclusive, because it had to be stopped at 285 ms after bounce, but its mean shock radius follows the two less well resolved and exploding counterparts very closely.

We also plot the non-exploding 1D model (solid black line) as well as an artificially exploded 1D case, whose explosion was triggered by decreasing the density in the infall layer ahead of the shock by a factor of 20, linearly growing from 500 km to 1500 km, at 300 ms after bounce. When the reduced mass infall rate reaches the shock, the shock begins to expand and starts running outward at  $\sim 400$  ms. The PNS left behind has nearly the same mass as the compact remnant formed in the exploding 3D models. We therefore used its long-time neutrino emission to define the time-dependent input for the neutrino HC scheme applied in model M.P3D.LS220\_m-HC, which extends the simulation of M.P3D.LS220\_m- to times later than 1.675 s after bounce.

In all models the shock reaches a maximum radius around 150 km at  $\sim 70$  ms post bounce, because it is first pushed outward by the initially high mass accretion rate, which rapidly adds a mantle layer around the forming NS, and then it is pulled inward by the settling and shrinking PNS radius when the mass accretion rate declines to values that cannot support further expansion. A second phase of shock expansion sets in when the Si/O composition interface falls into the shock at about 200 ms p.b. The strengthening of postshock convection by the 3D perturbations fosters the explosion of the models with 3D initial conditions; the corresponding physics was discussed by Müller et al. (2017a). In all models based on the 1D progenitor data we see a brief period of shock expansion, which transitions to a dramatic decrease after a second maximum of the shock radius. The subsequent quasi-periodic phases of large-amplitude shock expansion and contraction indicate the presence of strong SASI activity in the postshock layer. SASI has an intrinsic oscillation frequency of typically 50–100 Hz (corresponding roughly to the advection time scale through the gain layer), but SASI activity pushes the shock to larger radii until strong convection (a parasitic instability that taps energy from the SASI) sets in. This leads to cyclic phases of transient shock expansion and contraction. A similar behavior was observed in non-exploding  $20 M_{\odot}$  simulations by Glas et al. (2019b) and analysed in detail there.

The evolution of the mean shock radius shows close resemblance in all three exploding 3D models with no systematic resolution dependence. We interpret this finding as a consequence of the strong driving of postshock convection due to the large density and velocity perturbations in the O-shell of the collapsing 3D progenitor. In contrast, the non-exploding 3D models display a clear

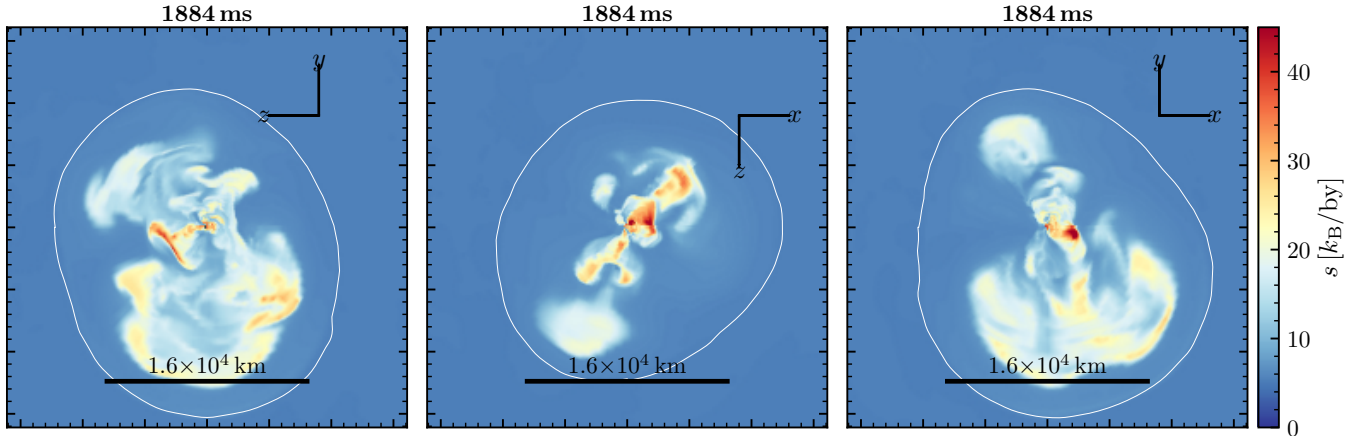


**Figure A2.** Entropy distributions in the  $y$ - $z$ ,  $x$ - $z$ , and  $x$ - $y$  planes of model L\_P3D\_LS220\_m- at the end of the 3D run with PROMETHEUS-VERTEX. The thin white line indicates the position of the shock.

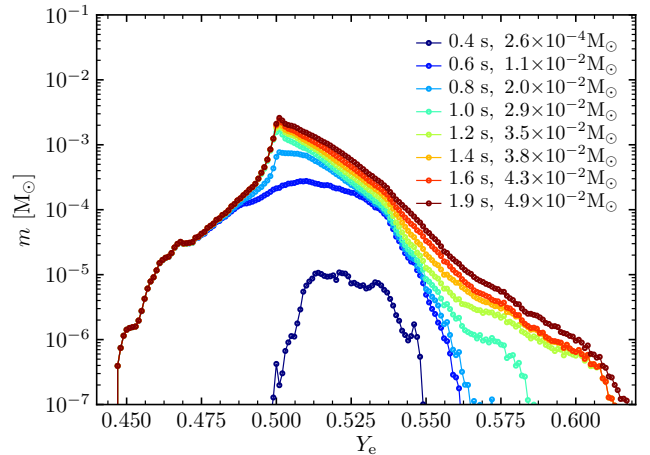
ordering of their mean shock radii, with larger excursions and higher maxima when the angular resolution is coarser. We explain this fact by stronger SASI activity in lower-resolution models, where the growth of parasitic Rayleigh-Taylor and Kelvin-Helmholtz instabilities is suppressed and the saturation amplitude of SASI is bigger (see also our discussion in Section 3.1).

Figure A2 presents the entropy distributions in three cut planes of the low-resolution model L\_P3D\_LS220\_m- at 1.884s after bounce. The explosion is highly asymmetric and exhibits the strongest shock expansion near the negative  $y$ -direction, closely resembling model M\_P3D\_LS220\_m- (see Figures 3, 4, and 5), despite structural differences in detail, for example an apparent tilting of the main axis of global deformation by about  $50^\circ$  in anti-clockwise direction in the  $x$ - $y$  plane (compare the right panel of Figure A2 with the middle and right panels of Figure 3). The fact that the biggest shock-pushing plume is in the negative  $y$ -hemisphere confirms our argument that higher ram pressure of the anisotropically collapsing 3D progenitor hampers shock revival and subsequent expansion in the opposite hemisphere.

Figure A3 displays the counterpart of Figure 8 for our simulation of L\_P3D\_LS220\_m-. The overall similarity is obvious, and also the low-resolution model fulfills the constraint that less than roughly  $10^{-4} M_\odot$  of neutrino-heated ejecta with  $Y_e \lesssim 0.47$  should be expelled in order to avoid an overproduction of  $N = 50$  nuclear species (Hoffman et al. 1996). Therefore also this model is compatible with the constraints deduced from the nucleosynthetic output of typical Type-II SNe.

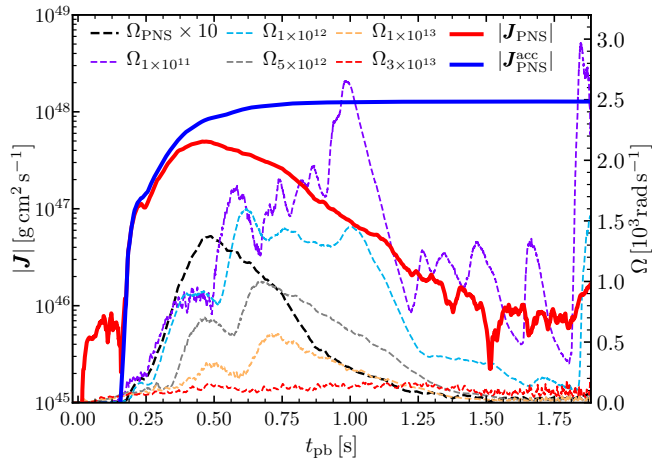
## B. ANGULAR MOMENTUM EVOLUTION

Figure B1 shows the analogue of the lower left panel of Figure 10 for model L\_P3D\_LS220\_m-. We witness a qualitatively similar behavior of all displayed quantities in the M and L models, independent of the angular resolution, with only smaller quantitative differences. In



**Figure A3.** Same as Figure 8, but for model L\_P3D\_LS220\_m-.

the lower-resolution model a deficit in the angular momentum stored in the PNS,  $|\mathbf{J}_{\text{PNS}}|$ , compared to the net inflow of angular momentum (inflow minus outflow),  $|\mathbf{J}_{\text{PNS}}^{\text{acc}}|$ , becomes visible somewhat earlier, starting at  $\sim 0.25$  s, than in model M\_P3D\_LS220\_m-, where the effect shows up only after roughly 0.3–0.35 s after bounce. The net angular momentum accreted onto the PNS is slightly smaller in model L\_P3D\_LS220\_m-, the angular momentum accumulated in the PNS also grows to a slightly lower peak with a value around  $5 \times 10^{47}$  ergs compared to  $\sim 7 \times 10^{47}$  ergs in model M\_P3D\_LS220\_m-. This maximum is reached at  $\sim 0.5$  s in the low-resolution model and is sharper than in model M\_P3D\_LS220\_m-, where a broad plateau of  $|\mathbf{J}_{\text{PNS}}|$  is visible between  $\sim 0.4$  s and  $\sim 0.75$  s. This implies that the decline from the peak sets in earlier in model L\_P3D\_LS220\_m-, but ultimately levels off to about the same value of roughly  $10^{46}$  ergs at  $\sim 1.5$  s post bounce. Correspondingly, the angular



**Figure B1.** Same as the lower left panel of Figure 10, but for model L.P3D.LS220.m-.

velocities in the accretion layer near the PNS surface as well as averaged over the PNS (assuming rigid rotation of the entire PNS mass) stay approximately 30–50% below those in model M.P3D.LS220.m-. These quantitative differences might suggest some influence of the angular resolution on the loss of angular momentum in the PNS surface layers discussed in Section 3.5.1. Alternatively, they could, however, also be a consequence of small differences in the downflow and accretion behavior, in course of which less matter with high angular momentum gets advected through the gain radius to reach the PNS surface. The low-resolution and higher-resolution models naturally differ in their detailed flow dynamics and their geometry of inflows and outflows because of the different resolution and stochastic variations in the explosion behavior (cf. our discussion around Figure A2).

In Figure B2 the evolution of the angular momentum on the computational grid is displayed as function of time for models M.P3D.LS220.m- (left) and L.P3D.LS220.m- (right). In both models the total angular momentum decreases roughly in the same way by approximately 5% (or  $\sim 10^{48}$  ergs) from an initial value of  $|\mathbf{J}_{\text{grid}}| \approx 2.147 \times 10^{49}$  ergs prior to the onset of stellar core collapse.<sup>6</sup> This is close to the drain of

<sup>6</sup> Although the stellar model is non-rotating and the computational grid covers the entire convectively perturbed O-shell, the pre-collapse angular momentum in the simulation volume,  $J_{\text{grid}} = |\mathbf{J}_{\text{grid}}| = |\int_{V_{\text{grid}}} dV \rho \mathbf{j}|$ , is not zero. This angular momentum has developed during the 7 minutes of our 3D simulation of convective burning in the oxygen shell (see Yadav et al. 2020). Although large by its absolute value, it accounts for only a few percent of the volume-integrated absolute value of the specific angular momentum times density, i.e., of  $\tilde{J}_{\text{grid}} = \int_{V_{\text{grid}}} dV \rho |\mathbf{j}|$ . The much bigger value of  $\tilde{J}_{\text{grid}}$  means that there is a lot more angular momentum in the system than  $\mathbf{J}_{\text{grid}}$  shows, since  $\tilde{J}_{\text{grid}}$  measures the angular momentum connected to small-scale variations and

angular momentum that we discuss in Section 3.5.1. Interestingly, the decline of the total angular momentum is slightly smaller in the lower-resolution model ( $\sim 1.04 \times 10^{48}$  ergs at the end of the simulation compared to  $\sim 1.26 \times 10^{48}$  ergs in model M.P3D.LS220.m-). This fact might be considered to be in conflict with an explanation of the angular momentum loss by numerical grid effects, potentially connected with the interfaces of the Yin and Yang patches of the grid. However, such a possibility cannot be ruled out, because the differences between models L.P3D.LS220.m- and M.P3D.LS220.m- could simply be a consequence of less accretion of high-angular-momentum matter into the extremely spinning, highly compressed near-surface layer of the PNS in the lower-resolution case, as mentioned above.

It is evident that the main reduction of the angular momentum happens in both models during the period of time when mass accretion leads to the extreme spin-up of the near-surface layers of the PNS. In both models there is a tight correlation of the growth of  $|\Delta \mathbf{J}_{\text{grid}}|$  with the time interval when the angular momentum in the PNS exhibits the dramatic decline (compare the black and red curves in the bottom panels of Figure B2). However, we do not observe any clear systematics in the temporal behavior of the three angular momentum components, neither with respect to angular resolution nor with the coordinate directions. Since flows near the  $y$ - $z$  plane cross Yin-Yang grid boundaries four times per full cycle, whereas flows close to the  $x$ - $y$  and  $x$ - $z$  planes cross Yin-Yang boundaries only twice per revolution, one would expect Yin-Yang-associated angular momentum loss to lead to a stronger damping of  $J_x^{\text{grid}}$  than of the other two angular momentum components. Indeed, we find a relative loss of  $J_x^{\text{grid}}$  of roughly 15% in both models, corresponding to a change from about  $-0.2 \times 10^{49}$  ergs to approximately  $-0.17 \times 10^{49}$  ergs, whereas  $J_y^{\text{grid}}$  and  $J_z^{\text{grid}}$  exhibit lower reductions, namely  $J_y^{\text{grid}}$  by  $\sim 8\%$  ( $\sim 6\%$ ) from  $-1.55 \times 10^{49}$  ergs to  $-1.44 \times 10^{49}$  ergs ( $-1.46 \times 10^{49}$  ergs) in model M.P3D.LS220.m- (L.P3D.LS220.m-), and  $J_z^{\text{grid}}$  by  $\sim 2\%$  from  $-1.46 \times 10^{49}$  ergs to approximately  $-1.44 \times 10^{49}$  ergs in both cases. The relative change of  $J_x^{\text{grid}}$  is therefore roughly twice the change of  $J_y^{\text{grid}}$  and seven to eight times the change of  $J_z^{\text{grid}}$ . Moreover, the absolute change of  $J_y^{\text{grid}}$  is several times that of  $J_z^{\text{grid}}$ , although both components are of similar magnitude initially. All of these facts seem to be in conflict with the symmetric treatment of flows on the

vorticity. Because of these vortex flows on small scales the total integral performed in  $\tilde{J}_{\text{grid}}$  is much larger than the total angular momentum added up vectorially, which causes numerical artifacts to grow more than the total might suggest. Therefore the angular momentum non-conservation during the pre-collapse evolution stayed within the numerical uncertainties that one can expect for 3D simulations of turbulent convection over several ten convective turnover cycles using a polar Yin-Yang grid.

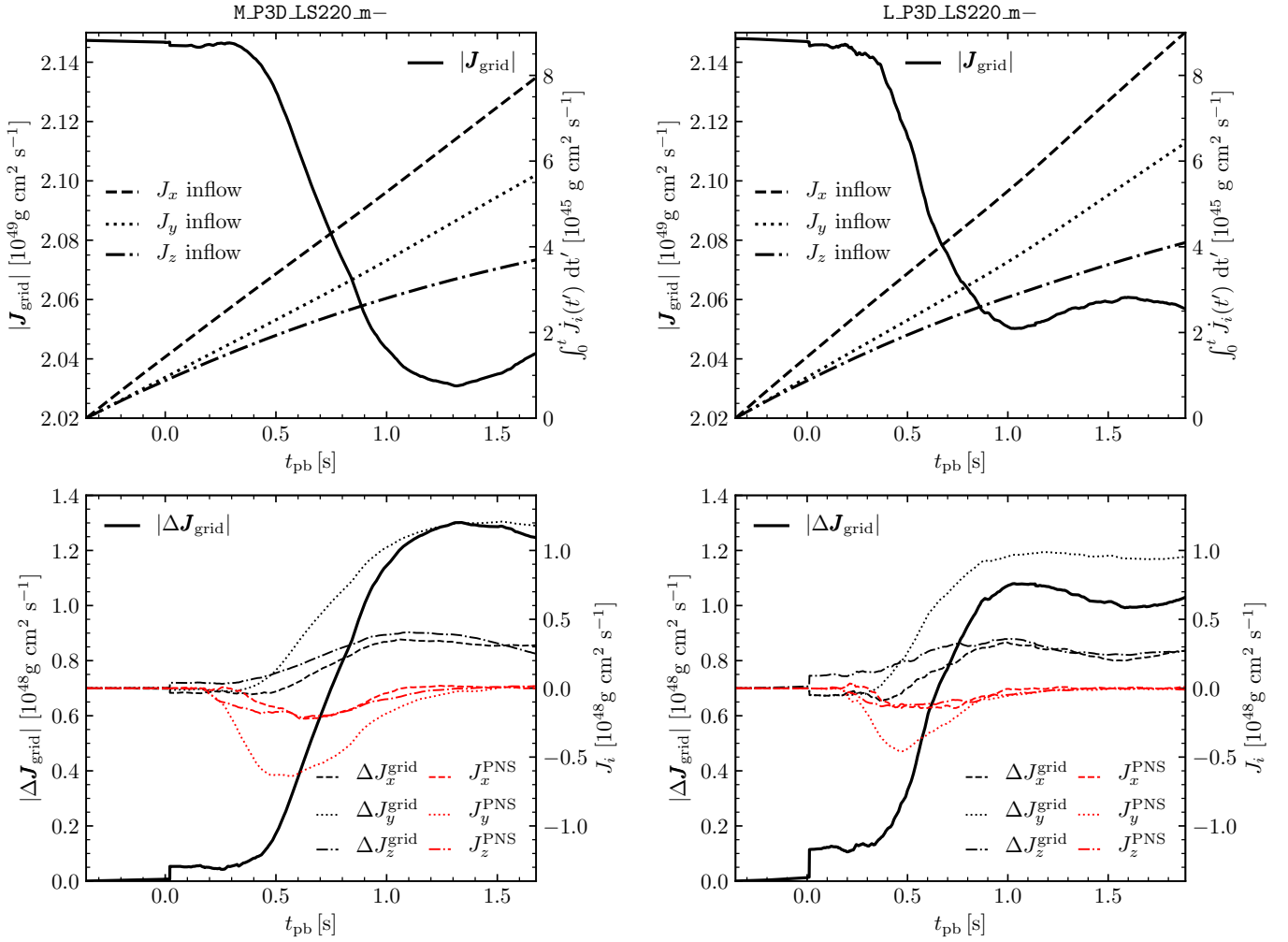


**Figure B2.** Angular momentum evolution for model M.P3D\_LS220\_m- (left) and model L.P3D\_LS220\_m- (right). *Upper panels:* Total angular momentum on the computational grid,  $|\mathbf{J}_{\text{grid}}|$  (solid line; left  $y$ -axis scale), and the vector components of the time-integrated inflow of angular momentum through the open outer radial boundary of the grid (dashed, dotted, and dash-dotted lines; right  $y$ -axis scale). The latter effect is miniscule and plays no relevant role in the total angular momentum budget. *Lower panels:* Change of the total angular momentum on the grid compared to the onset of core collapse,  $|\Delta\mathbf{J}_{\text{grid}}|$  (black solid line; left  $y$ -axis scale), change of the individual components of  $\mathbf{J}_{\text{grid}}$  compared to the initial values (black dashed, dotted, and dash-dotted lines; right  $y$ -axis scale), and components of the angular momentum contained by the PNS (red dashed, dotted, and dash-dotted lines; right  $y$ -axis scale). The discontinuous behavior at  $t_{\text{pb}} = 0$  is connected to a change of the numerical grid setup at core bounce and the corresponding mapping of the hydrodynamic quantities between the grids.

Yin and Yang patches of the grid and therefore seem to contradict a grid-connected explanation of the angular momentum loss. Since, however, there is a conservation law only for the total angular momentum but not for its individual components in 3D, the asymmetric evolution of  $J_y^{\text{grid}}$  and  $J_z^{\text{grid}}$  can be a consequence of torques due to hydrodynamic forces (and, in principle, also gravitational forces when 3D gravity effects play a role), shuffling angular momentum between the different components. In general, in complex 3D hydrodynamic flows such physical processes are always superimposed on possible numerical effects, for which reason there is no straightforward way to discern grid artifacts clearly

for conditions as they occur in the turbulent surroundings of the PNS.

Effects caused by the Yin-Yang grid can therefore not be diagnosed unambiguously. The higher relative change and the slightly later increase and earlier reduction of  $J_x^{\text{PNS}}$  compared to the other two PNS angular momentum components (Figure B2), as well as the differences in the evolution of  $J_y^{\text{PNS}}$  and  $J_z^{\text{PNS}}$ , may well be a consequence of the time evolution of the total angular momentum vector in the accretion flow instead of being connected to the Yin-Yang grid geometry. Clean test setups are therefore necessary to track down possible grid artifacts.

In the described 3D SN simulations the angular momentum is concentrated in an extremely rapidly revolving accretion layer near the surface of the PNS. This layer is geometrically narrow and contains a mass of only several  $10^{-2} M_{\odot}$ . Presently, we cannot attribute the drain of angular momentum from this region, which occurs over roughly 100 rotation periods, to any source — hydrodynamics solver, Yin-Yang grid, RbR+ transport and its coupling to the hydro, neutrino-mediated extraction of angular momentum— unambiguously. The tests of angular momentum conservation for the Yin-Yang grid in the literature (e.g., [Wongwathanarat et al. 2010](#), and references therein) are inconclusive for such conditions, because they never explored setups that came anywhere near the extreme situation obtained in the considered accreting PNSs with respect to densities and rotation rates. In our previous 3D core-collapse simulations of rotating progenitors ([Summa et al. 2018](#)) we could not witness any worrisome loss of angular momentum, but the simulated post-bounce evolution was not as long as in the current models and the angular momentum was also not concentrated in a narrow near-surface layer of the PNS.

Further dedicated and specifically designed tests of the angular momentum evolution on the Yin-Yang grid for our extreme PNS conditions are needed with and without neutrino transport. Such tests are being carried out with a new implementation of the Yin-Yang grid in the ALCAR code, which also contains a fully multi-dimensional treatment of the neutrino transport in addition to a RbR+ description ([Just et al. 2015](#); [Glas et al. 2019b](#)). But this is work in progress and beyond the scope of the present paper.

### C. ESSENTIALS OF LESA

The lepton-number self-sustained asymmetry (LESA) in the neutrino emission of new-born NSs was first discovered by [Tamborra et al. \(2014a\)](#) in 3D SN simulations of the Garching group with the PROMETHEUS-VERTEX code. It is defined by the development of a dominant dipole emission of the electron-neutrino lepton-number flux (number flux of  $\nu_e$  minus  $\bar{\nu}_e$ ), which can become larger than the corresponding monopole ([Tamborra et al. 2014a](#)). This implies that a hemispheric asymmetry of the electron fraction builds up inside the PNS, associated with the layer where PNS convection takes place highly anisotropically, carrying  $\nu_e$  out of the PNS core more efficiently in one hemisphere than in the opposite hemisphere. This can even lead to a dominant emission of  $\bar{\nu}_e$  on one side and  $\nu_e$  on the other side of the PNS. Such a lepton-number emission dipole is accompanied by a dipole of the total neutrino luminosity (i.e., of the sum of the luminosities of all species of neutrinos and antineutrinos) that points in the opposite direction and reaches an amplitude of only a few percent of the monopole on average (i.e., much lower than the LESA dipole relative to the lepton-number flux; [Tam-](#)

[borra et al. 2014a,b](#)). Because LESA can be found in models after the onset of the explosion, too, its origin is connected to the anisotropic convection in the interior of the PNS ([Glas et al. 2019a](#)). Therefore the LESA dipole has to be carefully discriminated from an accretion dipole of the lepton-number emission. This discrimination can be achieved by the criterion that the LESA is characterized by a temporal and spatial anti-correlation of the  $\nu_e$  and  $\bar{\nu}_e$  emission, whereas an accretion dipole exhibits a correlated behavior of the  $\nu_e$  and  $\bar{\nu}_e$  emission ([Tamborra et al. 2014b](#)). LESA was found to be considerably weaker in 3D simulations of the collapse of fast-spinning stellar cores ([Walk et al. 2019](#)). This can be understood from the fact that rapid rotation on the one hand damps the convective activity in the PNS due to the constraining influence of specific angular momentum conservation, which alters the large-scale structure of convective flows ([Janka et al. 2001](#)). On the other hand rapid differential rotation leads to shear effects in the neutrino advection and thus may destroy large-scale patterns of the radial neutrino transport in the optically thick regime.

The characteristic features of LESA, as diagnosed in the PROMETHEUS-VERTEX results of the Garching group, were discussed in a series of papers by [Tamborra et al. \(2014b\)](#); [Janka et al. \(2016\)](#); [Walk et al. \(2018, 2019, 2020\)](#), and [Stockinger et al. \(2020\)](#). Other groups confirmed the LESA phenomenon in their models and with different transport treatments (e.g., [O'Connor & Couch 2018](#); [Powell & Müller 2019](#); [Vartanyan et al. 2019](#); [Müller 2020](#); [Nagakura et al. 2021](#)). In a recent paper by [Glas et al. \(2019a\)](#) LESA properties were compared in simulations with RbR+ as well as fully multi-dimensional neutrino transport with the ALCAR code.

Because of the wealth of the previous literature, we will not describe the details of LESA once again here but refer the reader to the cited papers, also for a comparison of results from different groups and for suggestions to explain the physical origin of the LESA phenomenon (see in particular [Glas et al. 2019a](#) and [Müller 2020](#)). Instead of repeating such basic aspects, we will only present results in the following that are needed in support of our discussion of neutrino-induced NS kicks in Section 3.5.2.

For a quantitative analysis of the lowest-order multipoles (up to  $\ell = 3$ ) of LESA we follow the definitions by [Glas et al. \(2019a\)](#). The (complex) amplitude of a spherical harmonics mode  $(\ell, m)$  is defined as

$$c_{\ell}^m(r) = \sqrt{\frac{4\pi}{2\ell + 1}} \int_{4\pi} d\Omega r^2 F_{\nu,\text{lab}}^n(\mathbf{r}) Y_{\ell}^m, \quad (\text{C1})$$

where  $F_{\nu,\text{lab}}^n(\mathbf{r}) = F_{\nu_e,\text{lab}}^n(\mathbf{r}) - F_{\bar{\nu}_e,\text{lab}}^n(\mathbf{r})$  is the local (energy-integrated) lepton-number flux (density) of electron neutrinos minus antineutrinos in the laboratory frame of the observer,  $Y_{\ell}^m$  is the (complex) spherical harmonics of degree  $\ell$  and order  $m$ , and the integration

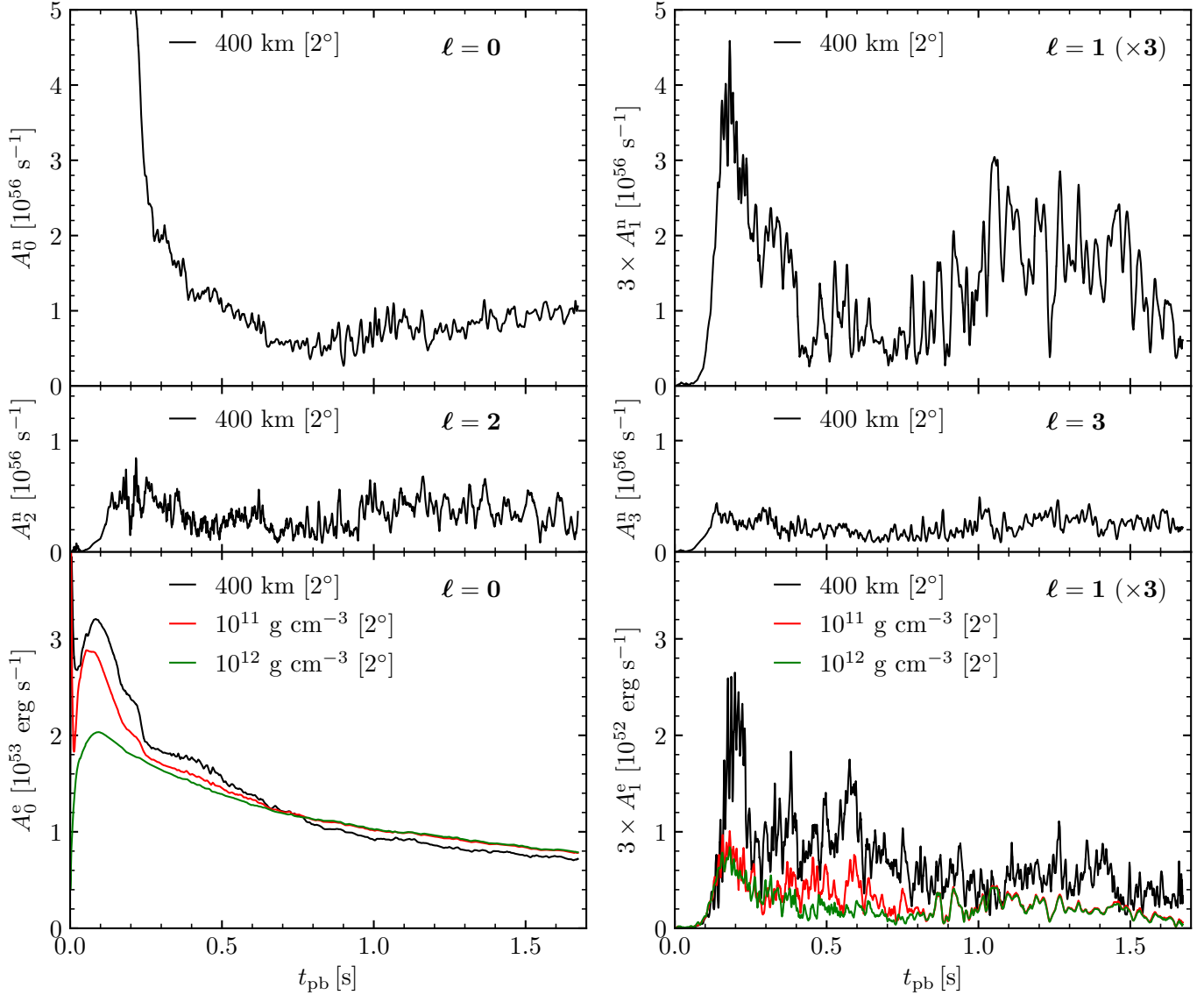


**Figure C1.** Multipole components of the neutrino emission in model `M_P3D_LS220_m-` with  $2^\circ$  angular resolution. The plotted data have been smoothed in a running window of 5 ms to damp short-time scale variations. *Upper four panels:* Monopole, dipole, quadrupole, and octupole ( $\ell = 0, 1, 2, 3$ ) of the electron-neutrino lepton-number emission. Note that the dipole amplitude as defined by Equation (C2) is scaled by a factor 3 for better comparison with the literature. Even ignoring this scaling, the dipole equals or even dominates the monopole after  $\sim 0.2$  s post bounce, whereas the quadrupole and octupole are considerably lower. This signals the presence of the LESA phenomenon. *Bottom two panels:* Monopole and dipole of the total neutrino energy emission. The monopole is the (all-sky) total neutrino luminosity given by the sum of the luminosities of all neutrino and antineutrino species. The dipole component (again shown as 3 times the amplitude of Equation (C2)) amounts to roughly 5% of the monopole on average. All quantities have been transformed to a distant observer in the lab frame. The black lines correspond to the analysis being performed in the free-streaming limit (at a radius of 400 km), the red lines in the bottom two panels show the results slightly above the neutrinospheres of  $\nu_e$  and  $\bar{\nu}_e$ , i.e., at a chosen density of  $10^{11} \text{ g cm}^{-3}$ , and the green lines represent the results slightly below the neutrinospheres of  $\nu_e$  and  $\bar{\nu}_e$ , i.e., at a density of  $10^{12} \text{ g cm}^{-3}$ .

is performed over the surface of a closed sphere at a chosen radius  $r$ . The amplitude of the  $\ell$ -mode,  $A_\ell(r)$ , is

defined by the following formula:

$$A_\ell(r) = \sqrt{\sum_{m=-\ell}^{m=+\ell} c_\ell^m c_\ell^{*m}}. \quad (\text{C2})$$



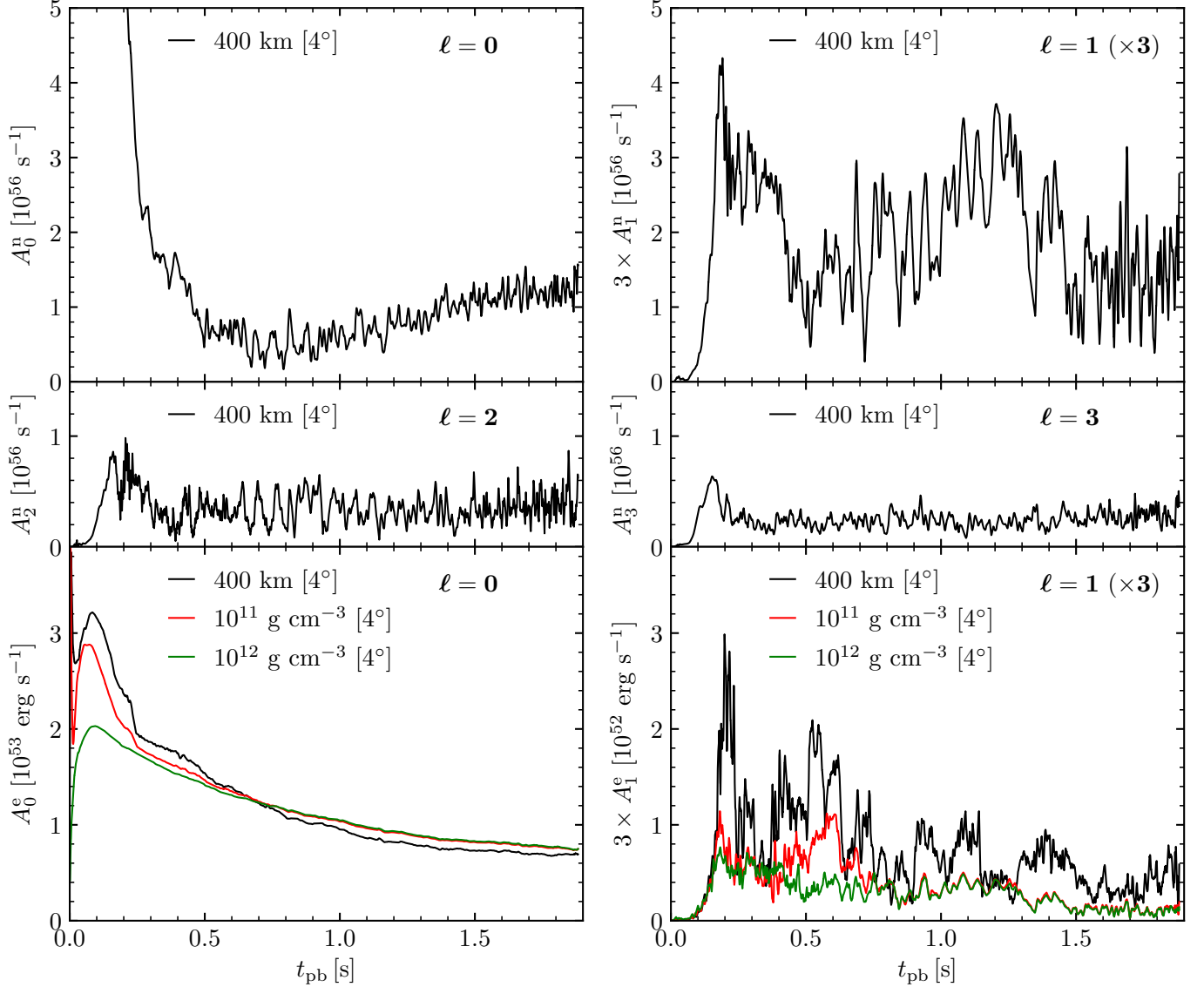


**Figure C2.** Same as Figure C1, but for model L\_P3D\_LS220\_m- with  $4^\circ$  angular resolution.

Figures C1 and C2 show the monopole, dipole (multiplied by a factor of 3 for direct comparison with Figure 3 in Tamborra et al. 2014a and Figure 1 in Glas et al. 2019a), quadrupole, and octupole of the electron lepton-number emission as functions of time (upper four panels) for models M\_P3D\_LS220\_m- and L\_P3D\_LS220\_m-, respectively. The bottom two panels display the monopole and dipole (again times 3) of the total energy flux defined as the sum of the energy fluxes of all neutrinos and antineutrinos:  $F_{\nu,\text{lab}}^e(\mathbf{r}) = \sum_{\nu_i} F_{\nu_i,\text{lab}}^e(\mathbf{r})$  with  $\nu_i = \nu_e, \bar{\nu}_e, \nu_\mu, \bar{\nu}_\mu, \nu_\tau, \bar{\nu}_\tau$ . The two monopoles represent, respectively, the total loss rate of electron lepton number through neutrino emission and the total neutrino luminosity of the PNS (as given, at 400 km, by the sum of all of the luminosities displayed in the right panel of Figure 1 for model M\_P3D\_LS220\_m-).

The basic features of LESA that are visible in Figures C1 and C2 are in line with the results of the previous PROMETHEUS-VERTEX models discussed in great detail in the literature cited above. However, there are also some special aspects due to the fact that the present models develop explosions in a fairly massive progenitor star and because we were able to continue the simulations to nearly 2 s after core bounce, thus much longer than before.

The onset of the explosion reduces the accretion of fresh material by the PNS. Since this material fuels the emission of large numbers of electron neutrinos in the process of its deleptonization, the monopole of the lepton-number emission declines much faster to values below  $10^{56} \text{ s}^{-1}$  in our present models than in the previous, non-exploding massive stellar progenitors (compare with Figure 3 in Tamborra et al. 2014a and Figure 1 in

Glas et al. 2019a). In fact, the decline is similarly fast as in exploding low-mass progenitors (see Figure 5 of Stockinger et al. 2020), which possess generically lower mass-infall rates and explode relatively fast. The characteristic LESA dipole of the electron neutrino lepton-number emission grows to a first maximum within about 0.2 s after bounce and a peak value very similar to the PROMETHEUS-VERTEX simulations discussed by Tamborra et al. (2014a), Janka et al. (2016), and Stockinger et al. (2020) and roughly compatible with results from simulations with the FORNAX code (Vartanyan et al. 2019), but somewhat faster and higher than in the simulations with ALCAR (Glas et al. 2019a) and FLASH (O’Connor & Couch 2018). The origin of these differences is most probably connected to differences in the development of convection inside the PNS in these simulations, which in turn can depend on resolution, geometry of the computational grid, numerical viscosity and order of the computational method, or on the details of the neutrino transport and neutrino interaction rates.

The dipole of the lepton-number flux displayed in the upper right panels of Figures C1 and C2 exceeds the monopole after 0.2–0.3 s post bounce. Its value plotted there is  $3A_1$  with  $A_1$  being the amplitude of Equation (C2). This follows the convention in Tamborra et al. (2014a); O’Connor & Couch (2018); Vartanyan et al. (2019), and Glas et al. (2019a) and represents the factor weighting the angular variation when the neutrino number and energy luminosities are written as sum of their monopole and dipole components as  $L_{\nu,\text{lab}}^{\text{n,e}} = A_0^{\text{n,e}} + (3A_1^{\text{n,e}}) \cos \theta$ .

After the initial peak the LESA dipole declines and exhibits a wide trough of lower values before it increases again after  $t_{\text{pb}} \sim 0.9$  s in model M\_P3D\_LS220\_m– and  $t_{\text{pb}} \sim 0.7$  s in model L\_P3D\_LS220\_m–. While the decrease of the dipole after the first maximum occurs on a similar time scale in both models, the increase out of the trough is different and seems to follow the somewhat different shape of the time evolution of the PNS angular momentum as visible in the lower left panel of Figure 10 and in Figure B1. The trough is deeper and wider in model M\_P3D\_LS220\_m–,<sup>7</sup> where the PNS angular momentum reaches higher values and declines more slowly from its plateau. We therefore hypothesize that there might be a causal connection, because Walk et al. (2019) witnessed that LESA is suppressed by rapid PNS rotation as mentioned above. Further analysis is needed

<sup>7</sup> Some features inside the troughs of both models, for example the local maximum between  $\sim 0.4$  s and  $\sim 0.8$  s in M\_P3D\_LS220\_m–, are connected to anisotropic accretion downflows onto the PNS, which produce mainly anisotropic  $\nu_e$  emission (and secondary  $\bar{\nu}_e$  emission) between the neutrinosphere and the gain radius. This can be verified by comparing the red and green lines in the bottom panels of Figures C1 and C2, because the former show the luminosities slightly above the neutrinospheres, the latter somewhat below the neutrinospheres of  $\nu_e$  and  $\bar{\nu}_e$ .

to test this hypothesis, but a detailed investigation is quite laborious and involved (see Walk et al. 2019) and is therefore deferred to future work.

LESA is present even after accretion onto the PNS has ended, which again supports its connection with anisotropic convection inside the PNS, in line with findings by Glas et al. (2019a); Powell & Müller (2019), and Stockinger et al. (2020). The late decline of the lepton-number dipole in both of our models after about 1.5 s post bounce may be connected with a weakening of PNS convection at these late times.

While the dipole of the lepton-number emission dominates the corresponding monopole for more than one second, the total energy luminosity has a much smaller asymmetry with a dipole component (again considered to be 3 times the amplitude  $A_1^e$  from Equation (C2)) that amounts to only  $\sim 5\%$  of the monopole (bottom panels of Figures C1 and C2). The acceleration of the PNS by a dipolar asymmetry of the neutrino emission scales according to  $\dot{v}_{\text{PNS}}^{\nu} \propto \frac{2}{3}(3A_1^e)$ . The 5% neutrino emission asymmetry includes a fluctuating and direction-variable contribution from anisotropic accretion flows, which produce anisotropic neutrino emission between neutrinosphere and gain radius, and it also includes anisotropic neutrino absorption by down- and outflows in the gain layer. The corresponding anisotropic neutrino absorption in ejecta material adds to the asymmetry of the neutrino energy flux at large radii. This contribution to the linear momentum of the escaping neutrinos is counterbalanced by linear momentum of the ejecta in the opposite direction (because the momentum transfer to the stellar plasma by the absorbed neutrinos is taken into account in our simulations), which implies that it is not transferred to the PNS.<sup>8</sup>

Once accretion by the PNS has ended and neutrino emission between the neutrinosphere and gain radius abates, the true neutrino-induced kick of the PNS depends on the anisotropic neutrino radiation that leaves the neutrinosphere. It is considerably smaller than the neutrino kick evaluated in the free-streaming limit (due to the mentioned anisotropic neutrino absorption in the gain layer), namely typically only about half of the total effect. This can be concluded from comparing the dipole amplitudes of the total neutrino luminosity in the free-streaming regime (e.g., at 400 km) and near the neutrinosphere (e.g., at  $10^{11}$  g cm<sup>-3</sup>) in the lower right panels of Figures C1 and C2. The neutrino-induced PNS kick velocity shown in the upper right panel of Figure 10 cor-

<sup>8</sup> Since the hydrodynamic PNS kick is computed as the negative of the linear ejecta momentum, it contains this fluid momentum received from neutrinos. The neutrino kick must therefore be evaluated in the free-streaming limit (and not at the neutrinosphere or at the gain radius) in order to account for the partial compensation of neutrino and gas momenta and thus to correctly compute the total PNS kick as the sum of neutrino kick and hydrodynamic kick.

responds to the total effect deduced from the neutrino luminosities in the free-streaming limit (as briefly mentioned in Section 3.5.2). The persistent dipole neutrino

emission until the end of our VERTEX simulations leads to a fairly constant PNS acceleration after  $\sim 1$  s post bounce, which however is dwarfed by the hydrodynamic kick (see Figure 10).

## REFERENCES

- Arnett, W. D. 1966, *Canadian Journal of Physics*, 44, 2553, doi: [10.1139/p66-210](https://doi.org/10.1139/p66-210)
- Arnett, W. D., & Meakin, C. 2011, *ApJ*, 733, 78, doi: [10.1088/0004-637X/733/2/78](https://doi.org/10.1088/0004-637X/733/2/78)
- Bethe, H. A., & Wilson, J. R. 1985, *ApJ*, 295, 14, doi: [10.1086/163343](https://doi.org/10.1086/163343)
- Blondin, J. M., & Mezzacappa, A. 2007, *Nature*, 445, 58, doi: [10.1038/nature05428](https://doi.org/10.1038/nature05428)
- Blondin, J. M., Mezzacappa, A., & DeMarino, C. 2003, *ApJ*, 584, 971, doi: [10.1086/345812](https://doi.org/10.1086/345812)
- Boggs, S. E., Harrison, F. A., Miyasaka, H., et al. 2015, *Science*, 348, 670, doi: [10.1126/science.aaa2259](https://doi.org/10.1126/science.aaa2259)
- Bollig, R., Janka, H. T., Lohs, A., et al. 2017, *PhRvL*, 119, 242702, doi: [10.1103/PhysRevLett.119.242702](https://doi.org/10.1103/PhysRevLett.119.242702)
- Bruenn, S. W., Lentz, E. J., Hix, W. R., et al. 2016, *ApJ*, 818, 123, doi: [10.3847/0004-637X/818/2/123](https://doi.org/10.3847/0004-637X/818/2/123)
- Buras, R., Janka, H.-T., Keil, M. T., Raffelt, G. G., & Rampp, M. 2003, *ApJ*, 587, 320, doi: [10.1086/368015](https://doi.org/10.1086/368015)
- Buras, R., Rampp, M., Janka, H.-T., & Kifonidis, K. 2006, *A&A*, 447, 1049, doi: [10.1051/0004-6361:20053783](https://doi.org/10.1051/0004-6361:20053783)
- Burrows, A., Hayes, J., & Fryxell, B. A. 1995, *ApJ*, 450, 830, doi: [10.1086/176188](https://doi.org/10.1086/176188)
- Burrows, A., Radice, D., Vartanyan, D., et al. 2020, *MNRAS*, 491, 2715, doi: [10.1093/mnras/stz3223](https://doi.org/10.1093/mnras/stz3223)
- Burrows, A., & Sawyer, R. F. 1998, *PhRvC*, 58, 554, doi: [10.1103/PhysRevC.58.554](https://doi.org/10.1103/PhysRevC.58.554)
- . 1999, *PhRvC*, 59, 510, doi: [10.1103/PhysRevC.59.510](https://doi.org/10.1103/PhysRevC.59.510)
- Burrows, A., & Vartanyan, D. 2021, *Nature*, 589, 29, doi: [10.1038/s41586-020-03059-w](https://doi.org/10.1038/s41586-020-03059-w)
- Chan, C., Müller, B., & Heger, A. 2020, *MNRAS*, 495, 3751, doi: [10.1093/mnras/staa1431](https://doi.org/10.1093/mnras/staa1431)
- Childs, H., Brugger, E., Whitlock, B., & et al. 2012, in *High Performance Visualization-Enabling Extreme-Scale Scientific Insight*, ed. E. Bethel (Boca Raton, FL: CRC Press), 357–372
- Colella, P., & Woodward, P. R. 1984, *Journal of Computational Physics*, 54, 174, doi: [10.1016/0021-9991\(84\)90143-8](https://doi.org/10.1016/0021-9991(84)90143-8)
- Colgate, S. A., & White, R. H. 1966, *ApJ*, 143, 626, doi: [10.1086/148549](https://doi.org/10.1086/148549)
- Collins, C., Müller, B., & Heger, A. 2018, *MNRAS*, 473, 1695, doi: [10.1093/mnras/stx2470](https://doi.org/10.1093/mnras/stx2470)
- Couch, S. M., Chatzopoulos, E., Arnett, W. D., & Timmes, F. X. 2015, *ApJL*, 808, L21, doi: [10.1088/2041-8205/808/1/L21](https://doi.org/10.1088/2041-8205/808/1/L21)
- Couch, S. M., & Ott, C. D. 2013, *ApJL*, 778, L7, doi: [10.1088/2041-8205/778/1/L7](https://doi.org/10.1088/2041-8205/778/1/L7)
- . 2015, *ApJ*, 799, 5, doi: [10.1088/0004-637X/799/1/5](https://doi.org/10.1088/0004-637X/799/1/5)
- Fryer, C. L., & Warren, M. S. 2002, *ApJL*, 574, L65, doi: [10.1086/342258](https://doi.org/10.1086/342258)
- . 2004, *ApJ*, 601, 391, doi: [10.1086/380193](https://doi.org/10.1086/380193)
- Fryxell, B., Müller, E., & Arnett, D. 1991, *ApJ*, 367, 619, doi: [10.1086/169657](https://doi.org/10.1086/169657)
- Fujibayashi, S., Takahashi, K., Sekiguchi, Y., & Shibata, M. 2021, arXiv e-prints, arXiv:2102.04467, <https://arxiv.org/abs/2102.04467>
- Gilkis, A., & Soker, N. 2014, *MNRAS*, 439, 4011, doi: [10.1093/mnras/stu257](https://doi.org/10.1093/mnras/stu257)
- Glas, R., Janka, H. T., Melson, T., Stockinger, G., & Just, O. 2019a, *ApJ*, 881, 36, doi: [10.3847/1538-4357/ab275c](https://doi.org/10.3847/1538-4357/ab275c)
- Glas, R., Just, O., Janka, H. T., & Obergaulinger, M. 2019b, *ApJ*, 873, 45, doi: [10.3847/1538-4357/ab0423](https://doi.org/10.3847/1538-4357/ab0423)
- Gossan, S. E., Fuller, J., & Roberts, L. F. 2020, *MNRAS*, 491, 5376, doi: [10.1093/mnras/stz3243](https://doi.org/10.1093/mnras/stz3243)
- Guilet, J., Sato, J., & Foglizzo, T. 2010, *ApJ*, 713, 1350, doi: [10.1088/0004-637X/713/2/1350](https://doi.org/10.1088/0004-637X/713/2/1350)
- Hempel, M., & Schaffner-Bielich, J. 2010, *NuPhA*, 837, 210, doi: [10.1016/j.nuclphysa.2010.02.010](https://doi.org/10.1016/j.nuclphysa.2010.02.010)
- Herant, M., Benz, W., Hix, W. R., Fryer, C. L., & Colgate, S. A. 1994, *ApJ*, 435, 339, doi: [10.1086/174817](https://doi.org/10.1086/174817)
- Hix, W. R., & Thielemann, F. K. 1999a, *Journal of Computational and Applied Mathematics*, 109, 321, <https://arxiv.org/abs/astro-ph/9906478>
- Hix, W. R., & Thielemann, F.-K. 1999b, *ApJ*, 511, 862, doi: [10.1086/306692](https://doi.org/10.1086/306692)
- Hoffman, R. D., Woosley, S. E., Fuller, G. M., & Meyer, B. S. 1996, *ApJ*, 460, 478, doi: [10.1086/176986](https://doi.org/10.1086/176986)
- Horowitz, C. J. 2002, *PhRvD*, 65, 043001, doi: [10.1103/PhysRevD.65.043001](https://doi.org/10.1103/PhysRevD.65.043001)
- Horowitz, C. J., Caballero, O. L., Lin, Z., O'Connor, E., & Schwenk, A. 2017, *PhRvC*, 95, 025801, doi: [10.1103/PhysRevC.95.025801](https://doi.org/10.1103/PhysRevC.95.025801)
- Janka, H. T. 2001, *A&A*, 368, 527, doi: [10.1051/0004-6361:20010012](https://doi.org/10.1051/0004-6361:20010012)

- Janka, H.-T. 2012, *Annual Review of Nuclear and Particle Science*, 62, 407, doi: [10.1146/annurev-nucl-102711-094901](https://doi.org/10.1146/annurev-nucl-102711-094901)
- Janka, H.-T., Kifonidis, K., & Rampp, M. 2001, in *Physics of Neutron Star Interiors*, ed. D. Blaschke, N. K. Glendenning, & A. Sedrakian, Vol. 578 (Springer Lecture Notes in Physics; Springer, Berlin), 333
- Janka, H.-T., Melson, T., & Summa, A. 2016, *Annual Review of Nuclear and Particle Science*, 66, 341, doi: [10.1146/annurev-nucl-102115-044747](https://doi.org/10.1146/annurev-nucl-102115-044747)
- Janka, H. T., & Müller, E. 1996, *A&A*, 306, 167
- Jerkstrand, A., Wongwathanarat, A., Janka, H. T., et al. 2020, *MNRAS*, 494, 2471, doi: [10.1093/mnras/staa736](https://doi.org/10.1093/mnras/staa736)
- Just, O., Obergaulinger, M., & Janka, H. T. 2015, *MNRAS*, 453, 3386, doi: [10.1093/mnras/stv1892](https://doi.org/10.1093/mnras/stv1892)
- Kazeroni, R., Guilet, J., & Foglizzo, T. 2017, *MNRAS*, 471, 914, doi: [10.1093/mnras/stx1566](https://doi.org/10.1093/mnras/stx1566)
- Kitaura, F. S., Janka, H. T., & Hillebrandt, W. 2006, *A&A*, 450, 345, doi: [10.1051/0004-6361:20054703](https://doi.org/10.1051/0004-6361:20054703)
- Kuroda, T., Arcones, A., Takiwaki, T., & Kotake, K. 2020, *ApJ*, 896, 102, doi: [10.3847/1538-4357/ab9308](https://doi.org/10.3847/1538-4357/ab9308)
- Lattimer, J. M., & Swesty, D. F. 1991, *NuPhA*, 535, 331, doi: [10.1016/0375-9474\(91\)90452-C](https://doi.org/10.1016/0375-9474(91)90452-C)
- Lentz, E. J., Bruenn, S. W., Hix, W. R., et al. 2015, *ApJL*, 807, L31, doi: [10.1088/2041-8205/807/2/L31](https://doi.org/10.1088/2041-8205/807/2/L31)
- Magkotsios, G., Timmes, F. X., Hungerford, A. L., et al. 2010, *ApJS*, 191, 66, doi: [10.1088/0067-0049/191/1/66](https://doi.org/10.1088/0067-0049/191/1/66)
- Marek, A., Dimmelmeier, H., Janka, H. T., Müller, E., & Buras, R. 2006, *A&A*, 445, 273, doi: [10.1051/0004-6361:20052840](https://doi.org/10.1051/0004-6361:20052840)
- Marek, A., & Janka, H. T. 2009, *ApJ*, 694, 664, doi: [10.1088/0004-637X/694/1/664](https://doi.org/10.1088/0004-637X/694/1/664)
- Martínez-Pinedo, G., Fischer, T., Lohs, A., & Huther, L. 2012, *PhRvL*, 109, 251104, doi: [10.1103/PhysRevLett.109.251104](https://doi.org/10.1103/PhysRevLett.109.251104)
- Melson, T., Janka, H.-T., Bollig, R., et al. 2015a, *ApJL*, 808, L42, doi: [10.1088/2041-8205/808/2/L42](https://doi.org/10.1088/2041-8205/808/2/L42)
- Melson, T., Janka, H.-T., & Marek, A. 2015b, *ApJL*, 801, L24, doi: [10.1088/2041-8205/801/2/L24](https://doi.org/10.1088/2041-8205/801/2/L24)
- Melson, T., Kresse, D., & Janka, H.-T. 2020, *ApJ*, 891, 27, doi: [10.3847/1538-4357/ab72a7](https://doi.org/10.3847/1538-4357/ab72a7)
- Müller, B. 2015, *MNRAS*, 453, 287, doi: [10.1093/mnras/stv1611](https://doi.org/10.1093/mnras/stv1611)
- . 2020, *Living Reviews in Computational Astrophysics*, 6, 3, doi: [10.1007/s41115-020-0008-5](https://doi.org/10.1007/s41115-020-0008-5)
- Müller, B., Heger, A., Liptai, D., & Cameron, J. B. 2016a, *MNRAS*, 460, 742, doi: [10.1093/mnras/stw1083](https://doi.org/10.1093/mnras/stw1083)
- Müller, B., & Janka, H. T. 2015, *MNRAS*, 448, 2141, doi: [10.1093/mnras/stv101](https://doi.org/10.1093/mnras/stv101)
- Müller, B., Melson, T., Heger, A., & Janka, H.-T. 2017a, *MNRAS*, 472, 491, doi: [10.1093/mnras/stx1962](https://doi.org/10.1093/mnras/stx1962)
- Müller, B., & Varma, V. 2020, *MNRAS*, 498, L109, doi: [10.1093/mnrasl/slaa137](https://doi.org/10.1093/mnrasl/slaa137)
- Müller, B., Viallet, M., Heger, A., & Janka, H.-T. 2016b, *ApJ*, 833, 124, doi: [10.3847/1538-4357/833/1/124](https://doi.org/10.3847/1538-4357/833/1/124)
- Müller, B., Tauris, T. M., Heger, A., et al. 2019, *MNRAS*, 484, 3307, doi: [10.1093/mnras/stz216](https://doi.org/10.1093/mnras/stz216)
- Müller, E., Fryxell, B., & Arnett, D. 1991, *A&A*, 251, 505
- Müller, E., & Steinmetz, M. 1995, *Computer Physics Communications*, 89, 45, doi: [10.1016/0010-4655\(94\)00185-5](https://doi.org/10.1016/0010-4655(94)00185-5)
- Müller, T., Prieto, J. L., Pejcha, O., & Clocchiatti, A. 2017b, *ApJ*, 841, 127, doi: [10.3847/1538-4357/aa72f1](https://doi.org/10.3847/1538-4357/aa72f1)
- Murphy, J. W., Dolence, J. C., & Burrows, A. 2013, *ApJ*, 771, 52, doi: [10.1088/0004-637X/771/1/52](https://doi.org/10.1088/0004-637X/771/1/52)
- Murphy, J. W., Mabanta, Q., & Dolence, J. C. 2019, *MNRAS*, 489, 641, doi: [10.1093/mnras/stz2123](https://doi.org/10.1093/mnras/stz2123)
- Nagakura, H., Burrows, A., Radice, D., & Vartanyan, D. 2019, *MNRAS*, 490, 4622, doi: [10.1093/mnras/stz2730](https://doi.org/10.1093/mnras/stz2730)
- Nagakura, H., Burrows, A., Vartanyan, D., & Radice, D. 2021, *MNRAS*, 500, 696, doi: [10.1093/mnras/staa2691](https://doi.org/10.1093/mnras/staa2691)
- Nakamura, K., Takiwaki, T., & Kotake, K. 2019, *PASJ*, 71, 98, doi: [10.1093/pasj/psz080](https://doi.org/10.1093/pasj/psz080)
- Nakamura, K., Takiwaki, T., Kuroda, T., & Kotake, K. 2015, *PASJ*, 67, 107, doi: [10.1093/pasj/psv073](https://doi.org/10.1093/pasj/psv073)
- Obergaulinger, M., & Aloy, M. Á. 2021, *MNRAS*, doi: [10.1093/mnras/stab295](https://doi.org/10.1093/mnras/stab295)
- O'Connor, E., & Ott, C. D. 2011, *ApJ*, 730, 70, doi: [10.1088/0004-637X/730/2/70](https://doi.org/10.1088/0004-637X/730/2/70)
- O'Connor, E. P., & Couch, S. M. 2018, *ApJ*, 865, 81, doi: [10.3847/1538-4357/aadcf7](https://doi.org/10.3847/1538-4357/aadcf7)
- Orlando, S., Miceli, M., Pumo, M. L., & Bocchino, F. 2016, *ApJ*, 822, 22, doi: [10.3847/0004-637X/822/1/22](https://doi.org/10.3847/0004-637X/822/1/22)
- Ott, C. D., Roberts, L. F., da Silva Schneider, A., et al. 2018, *ApJL*, 855, L3, doi: [10.3847/2041-8213/aaa967](https://doi.org/10.3847/2041-8213/aaa967)
- Papish, O., Nordhaus, J., & Soker, N. 2015, *MNRAS*, 448, 2362, doi: [10.1093/mnras/stv131](https://doi.org/10.1093/mnras/stv131)
- Papish, O., & Soker, N. 2011, *MNRAS*, 416, 1697, doi: [10.1111/j.1365-2966.2011.18671.x](https://doi.org/10.1111/j.1365-2966.2011.18671.x)
- . 2014, *MNRAS*, 438, 1027, doi: [10.1093/mnras/stt2199](https://doi.org/10.1093/mnras/stt2199)
- Plewa, T., & Müller, E. 1999, *A&A*, 342, 179, <https://arxiv.org/abs/astro-ph/9807241>
- Powell, J., & Müller, B. 2019, *MNRAS*, 487, 1178, doi: [10.1093/mnras/stz1304](https://doi.org/10.1093/mnras/stz1304)
- . 2020, *MNRAS*, 494, 4665, doi: [10.1093/mnras/staa1048](https://doi.org/10.1093/mnras/staa1048)
- Radice, D., Ott, C. D., Abdikamalov, E., et al. 2016, *ApJ*, 820, 76, doi: [10.3847/0004-637X/820/1/76](https://doi.org/10.3847/0004-637X/820/1/76)
- Rampp, M., & Janka, H.-T. 2002, *A&A*, 396, 361, doi: [10.1051/0004-6361:20021398](https://doi.org/10.1051/0004-6361:20021398)

- Rauscher, T., Heger, A., Hoffman, R. D., & Woosley, S. E. 2002, *ApJ*, 576, 323, doi: [10.1086/341728](https://doi.org/10.1086/341728)
- Reddy, S., Prakash, M., & Lattimer, J. M. 1998, *PhRvD*, 58, 013009, doi: [10.1103/PhysRevD.58.013009](https://doi.org/10.1103/PhysRevD.58.013009)
- Sawada, R., & Suwa, Y. 2021, *ApJ*, 908, 6, doi: [10.3847/1538-4357/abd476](https://doi.org/10.3847/1538-4357/abd476)
- Scheck, L., Kifonidis, K., Janka, H. T., & Müller, E. 2006, *A&A*, 457, 963, doi: [10.1051/0004-6361:20064855](https://doi.org/10.1051/0004-6361:20064855)
- Soker, N. 2020, *Research in Astronomy and Astrophysics*, 20, 024, doi: [10.1088/1674-4527/20/2/24](https://doi.org/10.1088/1674-4527/20/2/24)
- Steiner, A. W., Hempel, M., & Fischer, T. 2013, *ApJ*, 774, 17, doi: [10.1088/0004-637X/774/1/17](https://doi.org/10.1088/0004-637X/774/1/17)
- Stockinger, G., Janka, H. T., Kresse, D., et al. 2020, *MNRAS*, 496, 2039, doi: [10.1093/mnras/staa1691](https://doi.org/10.1093/mnras/staa1691)
- Sukhbold, T., & Adams, S. 2020, *MNRAS*, 492, 2578, doi: [10.1093/mnras/staa059](https://doi.org/10.1093/mnras/staa059)
- Sukhbold, T., Ertl, T., Woosley, S. E., Brown, J. M., & Janka, H. T. 2016, *ApJ*, 821, 38, doi: [10.3847/0004-637X/821/1/38](https://doi.org/10.3847/0004-637X/821/1/38)
- Sukhbold, T., Woosley, S. E., & Heger, A. 2018, *ApJ*, 860, 93, doi: [10.3847/1538-4357/aac2da](https://doi.org/10.3847/1538-4357/aac2da)
- Summa, A., Janka, H.-T., Melson, T., & Marek, A. 2018, *ApJ*, 852, 28, doi: [10.3847/1538-4357/aa9ce8](https://doi.org/10.3847/1538-4357/aa9ce8)
- Suwa, Y., Takiwaki, T., Kotake, K., et al. 2013, *ApJ*, 764, 99, doi: [10.1088/0004-637X/764/1/99](https://doi.org/10.1088/0004-637X/764/1/99)
- Suwa, Y., Tominaga, N., & Maeda, K. 2019, *MNRAS*, 483, 3607, doi: [10.1093/mnras/sty3309](https://doi.org/10.1093/mnras/sty3309)
- Takiwaki, T., Kotake, K., & Suwa, Y. 2014, *ApJ*, 786, 83, doi: [10.1088/0004-637X/786/2/83](https://doi.org/10.1088/0004-637X/786/2/83)
- Tamborra, I., Hanke, F., Janka, H.-T., et al. 2014a, *ApJ*, 792, 96, doi: [10.1088/0004-637X/792/2/96](https://doi.org/10.1088/0004-637X/792/2/96)
- Tamborra, I., Raffelt, G., Hanke, F., Janka, H.-T., & Müller, B. 2014b, *PhRvD*, 90, 045032, doi: [10.1103/PhysRevD.90.045032](https://doi.org/10.1103/PhysRevD.90.045032)
- Utrobin, V. P., & Chugai, N. N. 2011, *A&A*, 532, A100, doi: [10.1051/0004-6361/201117137](https://doi.org/10.1051/0004-6361/201117137)
- Utrobin, V. P., Wongwathanarat, A., Janka, H. T., et al. 2021, arXiv e-prints, arXiv:2102.09686. <https://arxiv.org/abs/2102.09686>
- . 2019, *A&A*, 624, A116, doi: [10.1051/0004-6361/201834976](https://doi.org/10.1051/0004-6361/201834976)
- Vartanyan, D., Burrows, A., & Radice, D. 2019, *MNRAS*, 489, 2227, doi: [10.1093/mnras/stz2307](https://doi.org/10.1093/mnras/stz2307)
- Walk, L., Tamborra, I., Janka, H.-T., & Summa, A. 2018, *PhRvD*, 98, 123001, doi: [10.1103/PhysRevD.98.123001](https://doi.org/10.1103/PhysRevD.98.123001)
- . 2019, *PhRvD*, 100, 063018, doi: [10.1103/PhysRevD.100.063018](https://doi.org/10.1103/PhysRevD.100.063018)
- Walk, L., Tamborra, I., Janka, H.-T., Summa, A., & Kresse, D. 2020, *PhRvD*, 101, 123013, doi: [10.1103/PhysRevD.101.123013](https://doi.org/10.1103/PhysRevD.101.123013)
- Wongwathanarat, A., Hammer, N. J., & Müller, E. 2010, *A&A*, 514, A48, doi: [10.1051/0004-6361/200913435](https://doi.org/10.1051/0004-6361/200913435)
- Wongwathanarat, A., Janka, H. T., & Müller, E. 2013, *A&A*, 552, A126, doi: [10.1051/0004-6361/201220636](https://doi.org/10.1051/0004-6361/201220636)
- Yadav, N., Müller, B., Janka, H. T., Melson, T., & Heger, A. 2020, *ApJ*, 890, 94, doi: [10.3847/1538-4357/ab66bb](https://doi.org/10.3847/1538-4357/ab66bb)
- Yasin, H., Schäfer, S., Arcones, A., & Schwenk, A. 2020, *PhRvL*, 124, 092701, doi: [10.1103/PhysRevLett.124.092701](https://doi.org/10.1103/PhysRevLett.124.092701)
- Yoshida, T., Takiwaki, T., Kotake, K., et al. 2019, *ApJ*, 881, 16, doi: [10.3847/1538-4357/ab2b9d](https://doi.org/10.3847/1538-4357/ab2b9d)